

**COMPUTATIONAL INVESTIGATION OF
HYDRODYNAMICS, MIXING AND
CRYSTALLIZATION IN A BATCH STIRRED
VESSEL**

Thesis

Submitted in partial fulfilment of the requirements for the degree of

DOCTOR OF PHILOSOPHY

By

LISTER HERINGTON FALLEIRO

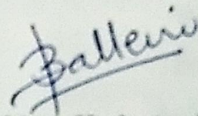
(Registration No: 155052CH15F06)



DEPARTMENT OF CHEMICAL ENGINEERING
NATIONAL INSTITUTE OF TECHNOLOGY KARNATAKA
SURATHKAL
OCTOBER, 2021

DECLARATION

I hereby *declare* that the Research Thesis entitled “ **Computational Investigation of Hydrodynamics, Mixing and Crystallization in a Batch Stirred Vessel** ” which is being submitted to the National Institute of Technology Karnataka, Surathkal in partial fulfilment of the requirements for the award of the Degree of **Doctor of Philosophy** in the **Department of Chemical Engineering**, is a *bonafide report of the research work carried out by me*. The material contained in this research thesis has not been submitted to any University or Institution for the award of any degree.



Lister Herington Falleiro

Registration number: 155052CH15F06

Department of Chemical Engineering

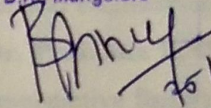
Place: NITK, Surathkal

Date: 22.10.2021

CERTIFICATE

This is to certify that the Research Thesis entitled “ **Computational Investigation of Hydrodynamics, Mixing and Crystallization in a Batch Stirred Vessel** ” submitted by **Mr. Lister Herington Falleiro** (Registration Number: 155052CH15F06) as the record of the research work carried out by him, is *accepted as the Research Thesis submission* in partial fulfilment of the requirements for the award of degree of Doctor of Philosophy.

DEPARTMENT OF CHEMICAL ENGINEERING
National Institute of Technology Karnataka, Surathkal
P.O. Srinivasnagar - 575 025, D.K. Mangalore


25/10/21

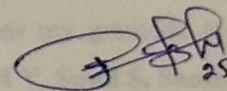
Research Guide

Dr. B. Ashraf Ali

Assistant Professor

Dept. of Chemical Engineering

NITK, Surathkal


25/10/21

Chairman- DRPC

Dr. P E Jagadeeshbabu.

Associate Professor and Head

Dept. of Chemical Engineering

NITK, Surathkal

HEAD OF THE DEPARTMENT
CHEMICAL ENGINEERING
National Institute of Technology Karnataka, Surathkal
P.O. Srinivasnagar - 575 025, D.K., Mangalore

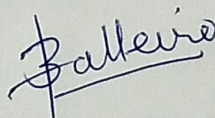
ACKNOWLEDGMENT

First and foremost, I express my heartfelt thanks and profound gratitude to my research supervisor, **Dr. B Ashraf Ali**, Chemical Engineering Department, for his esteemed guidance and kind support during my Ph. D., which has encouraged me to accomplish this research. In addition to the technical advice, his constant motivation, compassion, and encouragement during the moments of despair were behind the successful completion of my PhD thesis.

I am incredibly thankful to Research Progress Assessment Committee Members **Dr. A Kandasamy**, Department of MACS and **Dr. Vidya Shetty K**, Department of Chemical Engineering, NITK, for their insightful comments and critical suggestions. I acknowledge my thanks to the previous Head of Department of Chemical Engineering **Dr. Vidya Shetty**, **Dr. Raj Mohan B**, **Dr. Hari Mahalingam**, **Dr. Prasanna B. D** and current HOD **Dr. P. E. Jagadeeshbabu** for extending the administrative facility for tranquil progress of my PhD work. I express my heart full thanks to the Director of NITK Surathkal for providing the grants/funds to carry out this research work.

I also thank all the teaching and non-teaching staff of the Chemical Engineering Department, NITK, for their help and support during my PhD. I want to thank my dearest friends for their help during the research work. I want to thank our department's research scholars for the continuous encouragement, service, and support rendered during my research work. I would like to express my gratitude to **Ms. Anjana T**, **Manish B**, **Sriniketh A**, **Bharatesh K**, **Saiteja M V**, **Sunil S**, **Santosh K** and all my friends without whom this accomplishment would not have been possible.

I lovingly acknowledge my family for their invaluable cooperation and support during every single day of my life. They have always been a source of inspiration for me. Finally, I am grateful to everybody who has helped and encouraged me during my PhD.



LISTER HERINGTON FALLEIRO

DEDICATED
TO
MY FAMILY

ABSTRACT

In this work, the hydrodynamics, mixing and suspension quality of solids are numerically investigated using computational fluid dynamics (CFD). The transient CFD simulations are performed to obtain the flow field. Here multiple reference frame and sliding mesh approach are used to predict the flow field along with the standard $k-\varepsilon$ turbulence model. The velocity field is analyzed spatially and temporally, and liquid circulation is calculated at various impeller speeds to find an optimum impeller speed. To improve the flow field in a batch stirred vessel, various draft tube baffle configurations are introduced. The optimum baffle system (DTB-IV) is identified that supports liquid circulation, mixing and suspension of solids in the batch stirred vessel. It is found that suspension quality is strongly dependent on the prevailing hydrodynamics in the stirred vessel. Further, the optimised baffled stirred vessel (DTB-IV) is used to carry out the cooling crystallisation process. The primary difficulty in the design and scale-up of the crystallization process is the lack of understanding of the flow field, growth and nucleation at different scales. Here, the performance of an unbaffled stirred vessel is compared with a baffled stirred vessel system. To predict crystal size distribution (CSD) in batch stirred vessel system, the population balance equation (PBE) is used. The PBE is solved using the quadrature method of moments. The PBE accounts for both the size and the number of the particles, and it is coupled with the CFD model. This coupled algorithm integrates solubility data, nucleation and growth kinetics. To examine the crystallization process in a batch stirred vessel, potassium dihydrogen phosphate – water system is chosen. This is analyzed for unbaffled and baffled batch stirred vessel to quantify the growth and nucleation rates of the crystals. Further, the effect of seed mass, its size and temperature on the crystallization process is investigated. The results showed that baffled stirred vessel is more advantageous and supports the crystallization process.

Keywords: CFD, hydrodynamics, mixing, solid suspension, stirred vessel, batch crystallizer, PBE, crystal growth, nucleation.

NOMENCLATURE

List of Symbols and Units

Symbol	Description
kg	kilogram
mg	milligram
g	gram
m	meter
μm	micrometer
mm	millimeter
h	hour
min	minute
s	second
wt %	weight %
vol %	volume %
W	Watt
J	Joules
ρ	density
f	frequency
Hz	Hertz
$^{\circ}\text{C}$	degree Celsius
Pa	Pascal
C_{avg}	average concentration, kmol/L
$c^*(\theta)$	equilibrium concentration of solute

C_s^*	Critical seed size
d_{43}	De Brouckere mean diameter, m
d_{10}	Number Mean diameter, μm
k	turbulence kinetic energy, m^2/s^2
m_0	zeroth moment, $\#/\text{m}^3/\text{m}^3$
N	speed of the impeller, s^{-1}
t	time, s
L_s	seed size, μm
G	Growth rate, m/s
B	Nucleation rate, $\#/\text{m}^3 \cdot \text{s}$
R	Universal gas constant, J/mol. K
S	Relative supersaturation
T	Temperature, K
u	velocity, m/s

Greek letters

ρ	density of the fluid, kg/m^3
ρ_c	density of the crystal, kg/m^3
μ	viscosity of the fluid, Pa. s
Γ	Liquid circulation, m^2/s
μ_i^s	moments
σ	standard deviation
ν	kinematic viscosity of the fluid, m^2/s
θ	temperature, $^\circ\text{C}$

ABBREVIATIONS

CFD	Computational fluid dynamics
KDP	Potassium dihydrogen phosphate
QMOM	Quadrature method of moments
CSD	Crystal size distribution
BC	Boundary condition
MRF	Multiple reference frame
SM	Sliding mesh
RANS	Reynolds averaged Navier-Stokes
PBM	Population balance model
PBE	Population balance equations
DEM	Discrete element method
DPM	Discrete phase modelling
3D	Three dimensional
DTB	Draft tube baffles
KGTF	Kinetic theory of granular flows
EG	Euler- granular
SG	Specific gravity
COV	Coefficient of variation
UDF	User-defined function
SIMPLE	Semi implicit pressure linked equation

CONTENTS

ABSTRACT	I
NOMENCLATURE	III
CONTENTS	VII
LIST OF FIGURES	IX
LIST OF TABLES	XI
CHAPTER 1	1
1.1 INTRODUCTION	1
1.2 LITERATURE REVIEW	2
1.2.1 HYDRODYNAMICS IN STIRRED VESSELS	2
1.2.2 MIXING	4
1.2.3 SOLID SUSPENSION	6
1.2.4 CRYSTALLISER	8
CHAPTER 2	13
SCOPE AND OBJECTIVES OF THE WORK	13
2.1 SCOPE	13
2.2 OBJECTIVES	13
2.3 ORGANIZATION OF THE THESIS	14
CHAPTER 3	15
HYDRODYNAMICS AND MIXING IN A BATCH STIRRED VESSEL	15
3.1 INTRODUCTION	15
3.2 METHODOLOGY	16
3.2.1 GEOMETRY OF THE BATCH STIRRED VESSEL	16
3.2.2 CFD MODELLING	17
3.2.3 SIMULATION METHODOLOGY - SINGLE PHASE	18
3.3 RESULTS AND DISCUSSIONS	19
3.4 SUMMARY	30
CHAPTER 4	31
SOLID SUSPENSION IN STIRRED VESSELS	31
4.1 INTRODUCTION	31
4.2 METHODOLOGY	32

4.2.1 CFD MODELLING	32
4.2.2 SIMULATION METHODOLOGY – MULTIPHASE FLOW	39
4.3 RESULTS AND DISCUSSION	40
4.4 SUMMARY	46
CHAPTER 5	47
CRYSTALLIZATION IN STIRRED VESSELS	47
5.1 INTRODUCTION	47
5.2 METHODOLOGY	47
5.2.1 PHYSICAL PROPERTIES OF KH₂PO₄	47
5.2.2 CFD MODELLING	48
5.2.3 SIMULATION METHODOLOGY	51
5.3 RESULTS AND DISCUSSION	52
5.4 SUMMARY	62
CHAPTER 6	65
CONCLUSIONS	65
FUTURE SCOPE	67
REFERENCES	69
APPENDIX – I	79
APPENDIX – II	80
APPENDIX -III	82
RESEARCH PUBLICATIONS	86
BIODATA	88

LIST OF FIGURES

Figure 3.1 Schematic representation of the (a) unbaffled (b) baffled (c) 3D mesh for the baffled stirred vessel.	16
Figure 3.2. Contours of normalised velocity magnitude at different time instants 0s, 0.2s, 0.6s, 1s and 5s for the unbaffled (top row) and baffled stirred vessel (bottom row).	19
Figure 3.3 Temporal variations of velocity magnitudes at (a) point R and (b) point S	20
Figure 3.4 Comparison of CFD simulations with literature with normalized velocity magnitude (m/s) along a horizontal line at $z = -0.005$ m	21
Figure 3.5 Spatial variation of velocity magnitude (m/s) along a horizontal line $z = -0.005$ m	21
Figure 3.6 Effect of impeller speed on the (a) liquid circulation and (b) vorticity	22
Figure 3.7 (a) Spatial variation of turbulence viscosity (Pa.s) and (b) turbulence intensity (%) along a horizontal line $z = -0.05$ m	23
Figure 3.8 (a) Evolution of tracer concentration with time (b) Effect of impeller speed on mixing time	24
Figure 3.9 Contours of temperature distribution (a) unbaffled and (b) baffled stirred vessel	25
Figure 3.10 Spatial variation of water temperature along $z = -0.005$ m.	25
Figure 3.11 Schematic of various draft tube configurations used in the numerical investigation.	28
Figure 3.12 Contours of velocity magnitude for various draft tube configurations	29
Figure 4.1 Poincaré map for unbaffled (a) top view, (b) front view and baffled system (c) top view, (d) front view	40
Figure 4.2 Poincaré maps for different geometric modifications (a) DTB-I, (b) DTB-II, (c) DTB-III, (d) DTB-IV and (e) DTB-V	42
Figure 4.3 Poincaré maps of solids of different crystal density (a) 1300kg/m^3 , (b) 1770kg/m^3 , (c) 2340kg/m^3 and (d) 2750kg/m^3 for the top view (top row) and front view (bottom row)	43
Figure 4.4 Iso-contours of the volume fraction of solids ($Y = 0.005$ m).	44

Figure 5.1 Contours of supersaturation (a) unbaffled and (b) baffled stirred vessel	53
Figure 5.2 Contours of nucleation rate (a) unbaffled and (b) baffled stirred vessel	53
Figure 5.3 Temporal variation nucleation rate for the stirred vessel system	54
Figure 5.4 Temporal variation of the zeroth moment (m_0) of the stirred vessel systems	55
Figure 5.5 The crystal size distribution of the stirred vessel systems	56
Figure 5.6 Comparison of experimental data of growth rate and supersaturation with CFD simulations including and excluding shape factor (k_v) in the baffled stirred vessel	57
Figure 5.7 Effect of different seed mass on CSD	59
Figure 5.8 Effect of seed crystal size on the CSD.	60
Figure 5.9 Evolution of (a) nucleation and (b) growth rates for various seed crystal temperatures	61

LIST OF TABLES

Table 3.1 Effect of impeller blade angle on the liquid circulation, mixing time and power	26
Table 3.2 Effect of the multiple impellers on liquid circulation, mixing time and power	26
Table 3.3 Effect of the number of inner baffles on the liquid circulation, mixing time and power requirement	27
Table 3.4 Various draft tube baffle modifications used.	28
Table 3.5 Effect of geometric modification on liquid circulation and mixing time	29
Table 4.1 Shannon entropy and the uniformity in the stirred vessel	41
Table 4.2 Shannon entropy and the uniformity in the stirred vessel	42
Table 4.3 Shannon's entropy and the uniformity in the stirred vessel	44
Table 4.4 Mass uniformity index and cloud height for various draft tube configuration	45
Table 5.1 Physical properties of the solution and the crystals	48
Table 5.2 Statistical reports of the unbaffled and baffled stirred vessel system	56
Table 5.3 Effect of seed crystal amount on the mean size and crystallized mass	59
Table 5.4 Effect of seed crystal size on mean diameter, COV and crystallized mass	61
Table 5.5 Effect of seeding temperature on nucleation (B)/ growth (G)	62

CHAPTER 1

1.1 INTRODUCTION

Stirred vessels are simple in design, in which impellers are used for the generation of flow field and mixing. In such systems, the heat and mass transfer characteristics are observed to be significant. Hence, it is widely used in chemical, biochemical, petrochemical and allied industries such as batch processing of emulsions, crystallization and pharmaceutical applications (Gao et al. 2017).

However, due to the complex hydrodynamics of fluid phase mixing in such stirred vessels, many challenging problems still exist for improving the flow field and quality of mixing. The performance of stirred vessel is mainly influenced by the aspect ratio, type of impeller and its location, shape of the reactor and configuration of the baffle arrangement. The proper stirred vessel configuration is necessary to reduce inhomogeneity to achieve the desired process result and desired flow characteristics (Paul et al. 2004). Once proper stirred vessel configuration is identified, it is used for various industrial applications such as pharmaceuticals, catalytic, crystallization, sterilization and mineral industries (Mullin 2001).

The CFD modelling has been widely used to design suitable stirred vessel configuration (Wendt et al. 2009). The fluid phase mixing in stirred vessels reduces inhomogeneity present in the system, for example, reducing the non-uniformity of solid distributions in solid-liquid systems. The flow field in a stirred vessel has been modelled using several approaches (Joshi et al. 2011; Ashraf Ali et al. 2013; Vedantam and Ranade 2013). The rotation of the impeller is modelled using the multiple reference frame for steady-state and sliding mesh approach for transient simulations (Sommerfeld and Decker 2004; Ashraf Ali et al. 2013). The liquid phase turbulence is predicted using the standard $k-\epsilon$ turbulence model (Marshall and Bakker 2003; Joshi et al. 2011).

The performance of stirred vessel can be improved by improving the mixing characteristics in the vessel. It is desired to achieve uniform mixing at low operating costs (impeller speed). Mixing time is used as a parameter to quantify the degree of mixing in single-phase systems. For multiphase systems, it is desired to achieve a homogeneous regime of the two phases to maximize the heat and mass transfer. For

example, in the case of a solid-liquid system, the performance of the stirred vessel will improve based on the suspension characteristics and the mass transfer rate across the phases. Hence in order to achieve high mass and heat transfer in the vessel, complete suspension of the solids is preferred. Stirred vessels are used in industries for multiphase operations, such as crystallizer, catalytic reactors and polymerization reactor. A batch crystallizer is one of the complex multiphase system which is challenging to operate and achieve the expected quality of product.

Crystallization is used in process industries to achieve pure crystalline materials with a controlled size range and shape. These characteristics of the crystal control the downstream processing steps such as filtration and drying (Szilágyi and Nagy 2018). The quality of crystals strongly depends on various operating conditions in a crystallizer such as local supersaturation, hydrodynamics, fluid mixing, and geometry, modes of crystallizer operation, seeding, aggregation, breakage and hence the crystal size distribution (CSD) (Rohani et al. 2005a; de Souza et al. 2021).

In a stirred vessel, the energy dissipation is high due to large local gradients. Various types of impellers and baffles were used to produce different flow patterns and mixing. The hydrodynamics of a given system with kinetics influences scale up in the crystallization process. Hence, finding an optimum configuration of the stirred vessel is crucial that supports the desired CSD.

1.2 LITERATURE REVIEW

The stirred vessel is most widely used equipment for design of industrial process. The hydrodynamics of fluid phase mixing in batch stirred vessel is one of the challenging issues and it improves product quality. The computational fluid dynamics (CFD) tool is used to predict the local hydrodynamics and phase distributions, thus proper design of stirred vessel system. Here overview of CFD modelling of stirred vessel is briefly discussed in the forthcoming sections.

1.2.1 Hydrodynamics in stirred vessels

Ranade et al. (1992) investigated eight axial impellers using Laser Doppler anemometry (LDA). The simulation predictions showed good agreement with

experiments. The flow was compared in terms of mean velocity, turbulence parameters near the impeller region. They found that the two-equation $k-\varepsilon$ turbulence model is accurate enough to predict the bulk flow in all the axial impellers.

Zhou and Kresta (1996) studied the energy dissipation of different types of impellers. Laser Doppler anemometry (LDA) was used to measure the mean and root-mean-square velocity (RMS). It was found that the fluid foil turbine (A310) was the most efficient in generating convective flow.

Houcine et al. (2000) investigated different geometric modifications on the shapes of the vessel and the vessel internals for low Reynolds number ($Re > 110$). An optimum geometry was recommended based on the power consumption per unit mass for the same mixing efficiency for each type of stirrer.

Aubin et al. (2001) analyzed the flow patterns of axial impellers. Laser Doppler Velocimetry (LDV) was used to analyze the radial, axial and tangential velocity components. Low velocities were observed in the upper part of the tank for down pumping impellers (pitched blade turbine).

Kumaresan and Joshi (2006) investigated the hydrodynamics of the impeller blades angle, width, twist, thickness, pumping direction and number of blades in a stirred vessel. The flow patterns were compared based on the flow number and power consumption in the vessel. The CFD simulations were validated through LDA measurements for various impeller modifications in the vessel. Hence CFD model can be used to model different alterations on the internals of the stirred vessel.

Ochieng et al. (2008) investigated the flow field in a stirred vessel with a Ruston turbine impeller (RT). Due to the draft tube's presence, the two circulation loops usually generated by the RT are converted to a single circulation loop in the axial direction. The presence of the draft tube reduces the mixing time by 50%.

Ashraf Ali et al. (2013) numerically investigated the hydrodynamics in a baffled stirred vessel. They reported that 24 L is the optimum volume required to ensure sufficient liquid height above the draft tube.

Yoshida et al. (2015) studied the effect of the presence of the baffles in the stirred vessels to avoid the formation of a vortex. Particle image velocimetry (PIV) was used to evaluate the velocity profiles in the stirred vessel. They reported that the

presence of the baffles reduced the energy consumption and improved the convective flow patterns.

Dong et al. (2016) studied the change in the velocity distribution due to the shape of the vessel bottom and the baffle length in the stirred vessel. The dished bottom was recommended to avoid dead zones at the circumference in flat bottom vessels.

1.2.2 Mixing

Tatterson (1982) investigated the effect of the draft tube on the circulation and mixing studies. The performance of the stirred vessel improves due to the presence of the draft tube along with wall baffles than the standard four-wall baffle configuration. Further, it is found that placing the impeller inside the draft tube improves the performance of circulation and mixing.

Sahu et al. (1999) investigated the mixing in a stirred vessel for five different axial flow impellers designs. It was found that the dissipation rate estimated using the RMS velocity and length scale through autocorrelation was comparatively poor with respect to CFD predictions. They proposed a new method (zonal modelling) to calculate the turbulence dissipation rate values, giving excellent agreement between dissipation rate and CFD predictions. They further extended the predicted flow field to model the mixing process and calculated the mixing time in excellent agreement with experimental measurements. They considered the mixing time as the time which measures the tracer concentration to reach 95% of the final concentration. The accuracy of the results is improved by creating a zone around the impeller region. There are high - velocity fluctuations.

Patwardhan and Joshi (1999) investigated the relationship between the flow pattern and mixing for 40 axial flow impellers using LDV and CFD measurements. It was found that the mixing time (θ) varies inversely to the flow number of the impeller. The CFD predictions showed that the same mixing could be achieved by reducing the eddy diffusivity by 20%, and there is a substantial saving in operating costs.

Oshinowo et al. (2001) simulated mixing time using computational fluid dynamics (CFD) in a stirred vessel. They found that empirical correlations derived from experiments have many limitations. Generally, the small-scale vessels are used to

perform experiments, and the geometry of the impeller may not exactly be the same in the full scale stirred vessel. However, the feed location of the tracer is relative to the impeller location, and it will be different for lab-scale and large scale stirred vessels. These factors are responsible for getting significant inaccuracies in the mixing time calculations. They also reported two methods to evaluate the mixing time. The first technique uses the tracking of neutral buoyant tracer particles. The particles were tracked with turbulent dispersion, and the concentration was measured at various time instants. In the second technique, the liquid tracer was added near the liquid surface, and the tracer concentrations were monitored at different locations in the vessel with time. It was found that the concentration of the tracer oscillates with time. The mixing time was defined as the time taken for the uniformity to reach a value of 0.99. They found that the RSM turbulence model fits the velocity distribution better than the $k-\epsilon$ turbulence models in the vessel for pitched blade and Ruston turbine impellers.

Ochieng and Onyango (2008) investigated the bottom clearance of the impeller in stirred vessels. They reported that the power number itself is not sufficient to optimise the geometry of the stirred vessels. Therefore, they introduced a new term, homogenisation energy, dependent on two parameters: impeller power and mixing time. They found that for low impeller clearance, the homogenisation energy was minimal. The homogenisation energy was further reduced by introducing a draft tube in the stirred vessel.

Al-Qaessi and Abu-Farah (2009) predicted the mixing time for miscible liquids through CFD in batch reactors and validated with experimental data. They found that CFD predicts the mixing time accurately even for high viscosity liquid mixtures.

Coroneo et al. (2011) studied the effect of RANS based CFD simulations on the fluid mixing in a stirred vessel. They found that the error in the predictions can be reduced by decreasing the size of the control volumes (finer grids). The mixing time estimated through CFD simulations is accurate for smaller grid size, reducing the numerical diffusion in the computations.

Weinekötter and Gericke (2013) reported that the mixing time in a batch system is calculated by introducing the tracer and sampling the variation at different locations in the vessel. Hence monitoring the tracer concentration at other spatial locations with time gives accurate mixing time predictions.

Aydin and Yapici (2018) investigated the mixing time in a stirred vessel using the electrochemical limiting diffusion current technique (ELDCT). It was found that the local mixing time varies depending on the measurement location and the accuracy of the mixing time improves with more number sensors. Hence the mixing time obtained through experimental methods is difficult and expensive, and many measuring probes are necessary to achieve a reliable mixing time.

Torotwa and Ji (2018) studied the mixing performance of different impeller designs in the stirred vessel through CFD since it is difficult to obtain accurate information on the turbulence generated by the impeller rotation. The standard k- ϵ turbulence model along with the Multiple reference frame (MRF) approach was used. The CFD simulations for different impellers were validated with experimental values. They found that the mixing performance is improved by selecting a suitable impeller design that generates energy to create turbulence in the stirred vessel. The turbulent diffusivity can be used for optimizing different strategies of stirred vessels.

1.2.3 Solid Suspension

Chudacek (1985) investigated the solids suspension in a flat bottom stirred vessel. The abrupt change in the flow patterns due to the flat bottom at the center and the periphery of the stirred vessel causes the accumulation of suspended solids at the corners and the central region below the impeller. Hence it was recommended to have a profiled bottom to obtain a complete suspension. Therefore, the flow patterns in the bottom of the vessel control the suspension of solids.

Kasat et al. (2008) numerically investigated the solid suspension and its impact on the liquid mixing in a stirred vessel. Two fluid models with mixture properties were used to simulate liquid-solid flow in the stirred vessel. The mixture turbulence was predicted using the standard k- ϵ turbulence model. The mixing time was calculated using the tracer technique for various impeller rotational speeds. They found that the mixing time gradually drops with an increase in the rotational speed. They also concluded a delay in the mixing because of very low liquid velocities at the top of the vessel, thereby creating dead zones in the stirred vessel.

Tamburini et al. (2009) investigated dense suspension in a baffled stirred vessel with a Rushton turbine (RT) impeller. The Eulerian-Eulerian model with the $k-\varepsilon$ turbulence model is used to simulate the solid-liquid system. The simulation was validated by comparing the solid concentration with experiments through image processing techniques.

Ochieng and Onyango (2010) reviewed the numerical simulations of solids suspension in stirred vessels. They found that researchers have focused on the off-bottom suspension through experiments that are not accurate and does not account for dead zones in the vessel. They reported that computational fluid dynamics could be used to simulate solid suspension and quantify the quality of the suspension through size distribution and cloud height.

Vedantam and Ranade (2013) reported that in multiphase operations involving solids and liquids, it is essential to maintain solids in suspension to enhance mass transfer rate between the phases. The solids are lifted from the bottom of the vessel due to the kinetic energy generated by the rotation of the impeller. This energy creates a turbulent flow field due to which the solid particles are lifted from the vessel base and subsequently dispersed and distributed throughout the vessel. The minimum energy required to ensure the complete off-bottom suspension is known as just suspension speed.

Ashraf Ali et al. (2013) numerically investigated the hydrodynamics and crystal motion in a baffled stirred vessel. They found that the volume of the vessel, impeller speed and injection location of the solids affect the performance of the stirred vessel.

Tamburini et al. (2014) numerically investigated the influence of drag and turbulence on the suspension characteristics in the stirred vessel. In this work, two baffled stirred vessels were simulated using the Eulerian-Eulerian Model (E-E) with MRF or Sliding mesh approach. They found that for dense solid loading, the turbulence fluctuations lead to deviations from the experimental data. The turbulence dispersion force needs to be accounted for to capture the physics of the system.

Mishra and Ein-Mozaffari (2020) carried out a comprehensive review of solid-liquid mixing. They found that factors such as power required, mixing time, quality, and quantity are considered while designing a stirred vessel. The just suspension criteria (Zwietering correlation) are not sufficient for the perfect mixing of solids. Further

research is required to predict the solid suspension for a scale-up process. It is found that the thorough literature is not available for high solid loading concentrations in Newtonian fluids.

1.2.4 Crystalliser

Batch crystallizer is used primarily for crystallization in the production of fine chemicals, pharmaceuticals, dyestuffs, and other specialty chemicals. They handle a relatively small volume of materials, ranging from 0.02 to 20 m³. They operate transiently therefore, supersaturation and other process variables vary significantly in an uncontrolled batch operation, resulting in excessive nucleation and undesirable product quality (Mersmann 2001).

In batch crystallizers, control is achieved using (a) improved mixing at the macroscale and molecular level in the case of crystallization processes, which often have a short reaction time in the order of a few milliseconds, (b) optimal cooling rate to generate constant supersaturation during a batch operation, (c) seeding with a narrow distribution of product crystals, and (d) fines dissolution (Mersmann 2001).

Good bulk mixing can be provided by improving the crystallizer configuration (e.g., by inserting baffles and draft tubes, by appropriate selection of the location of the feed pipes, and by increasing the agitation rate and using high-efficiency impellers with high pumping capacity) (Baldyga and Bourne 1984a). The resulting increase in the secondary nucleation rate due to the high shear rate is less than the increase in spontaneous nucleation due to poor mixing in the regions of high supersaturation at feed entries in reactive crystallization or close to the cooling surfaces in cooling crystallizers (Mersmann 2001).

Kramer et al. 1999 reported that whenever there is a difference in material density of the solid and liquid phase, particle segregation will occur to some extent that depends on the internal circulation rate, which is related to the specific power input of a circulation pump or impeller. The stirred vessel type crystalliser is considered since it the simplest crystalliser in which the product size can be maintained easily. When dealing with agitated vessels, an axial flow from the stirrer to the bottom is recommended, and a draft tube (DT) is favourable to operate the crystalliser with the

minimum specific power input (ϵ) min, which is smaller than in a vessel without this tube. Baffles are necessary to avoid a deep vortex at a high stirrer Reynolds number (Mersmann 2001).

Crystal dynamics depends on four basic phenomena, namely nucleation, growth, breakage and aggregation of crystals. Crystal growth and nucleation kinetics strongly depend on solution supersaturation, temperature and hydrodynamics that are system-specific. It is challenging to find optimal operating conditions that yield desired product quality and associated crystal size distribution. This happens when the scale of crystallizer changes from lab to pilot or industrial scale (Green, 2002; Paul et al., 2004). However, it is necessary to resolve the spatial velocity distribution and then resolve the fluid particle and particle-particle interactions.

Kougoulos et al. (2005) investigated the mixing and heat transfer in a batch crystallizer through the compartmental model. The crystallizer was divided into several compartments. Each compartment was assumed to be homogeneous in terms of momentum, heat and mass transfer. The process modelling software gPROMS was used, which combines the hydrodynamics data from CFD simulation with crystal population, mass, and energy balances, including the crystallization kinetics within each compartment. Their main aim was to overcome the shortcomings of CFD in a batch cooling crystallization because of its transient nature, i.e., change of system temperature with time. It was challenging to integrate a complete developed population balance model environment in CFD and predict the crystal size distribution (CSD).

It is important to generate a uniform and mild supersaturation within the crystallization magma (i.e., a uniform distribution of solute molecules or ions and negligible temperature gradient at the macro-scale and molecular level) during crystallization. Moreover, a uniform solids suspension density provides homogeneous distribution of crystal area for growth within the bulk solution (Myerson et al., 2019). If the local supersaturation is high where there is a deficiency of KDP crystal surface area for growth, spontaneous nucleation will initiate and lead to small mean crystal size and a broad CSD (M. S. Joshi, 1974). At very high local supersaturation, excessive nucleation occurs even in the presence of crystals. Accurate numerical modelling of crystallization requires suitable models for fluid dynamics in the crystallizer and for

representing the key phenomena, such as nucleation, growth and breakage. Those models have then to be coupled and taken into account simultaneously

Primary nucleation is a first step that occurs due to the high supersaturation of the solute in the crystallizer. The final crystal product obtained is non-uniform, polymorphic and fine powder in nucleation dominated process (N. Doki et al., 2001; Wei et al., 2001; Liiri et al., 2010).

Seeding with a narrow distribution of product crystals prevents spontaneous nucleation and improves CSD (Doki et al. 2001). The time of addition of seed crystals is very critical. It should be at the start of the operation to avoid spontaneous nucleation. If proper and sufficient seeding is utilized, spontaneous nucleation may be avoided even when a natural cooling policy is employed, leading to a unimodal distribution of the final crystal mass. (Mersmann 2001)

The quantitative data on seeding is constrained in deciding what number of and what size of seeds ought to be acquainted into a crystalliser with create item crystals of the required size. (Doki et al. 1999). The quantitative information on seeding is limited in determining how many and what size of seeds should be introduced into a crystallizer to produce product crystals of the desired size. So far, there is no methodology available for this purpose. (Doki et al. 1999)

Doki et al. (2001) studied the seeding of potassium alum through natural and controlled cooling in a batch crystallizer. It was found that at low seed concentration, bimodal CSD was obtained due to secondary nucleation irrespective of the cooling method used. In the natural cooling mode, the mean size of the crystal was smaller than the controlled cooling mode due to intensive secondary nucleation. It is also found that for high seed concentrations, the cooling mode does not play a significant role, and the CSD obtained was unimodal with the same mean sizes.

Rohani et al. (2005) investigated that the quality of the product obtained from the crystallization process is measured in terms of the crystal size distribution (CSD), its morphology, the polymorphic forms obtained and the purity of the crystals and the crystalline structure along with the yield of the product. The flowability and the crystal density is related to the CSD. The desired CSD is obtained by controlling the operating conditions such as the local supersaturation, solvent type, operating temperature, degree of homogeneity, internal vessel geometry and the seeding policies.

Rohani et al. (2005b) studied the effect of external techniques to achieve the desired CSD. They found that by using a feedback control system, the desired CSD may be achieved. Secondly, optimal control of the cooling policy can be used to achieve the desired CSD.

Kubota and Onosawa (2009) experimentally investigated the crystallization of ammonium aluminum sulfate (AAS) and water system. They introduced seeds having mass more than the critical mass required to suppress secondary nucleation into the crystallizer. There was no temperature control policy used for this system. The CSD obtained was narrow and unimodal. They found that without any prior knowledge of the crystal growth and nucleation kinetics, a natural cooling profile and control system, a unimodal CSD is obtained by adding seeds into the crystallizer.

Liiri et al. (2010) investigated hydrodynamics in a crystallizer in order to better understand crystal growth. Wei et al. (2001) discussed transient super-saturation distribution in a 3D crystallizer and the effect of feed locations and impeller speed on mixing and CSD in precipitation.

Y. Tseng et al. (2014) numerically investigated 43 crystallization systems and reported a high discrepancy in the critical seed mass calculated based on the single correlation. It is insufficient to define the connection between critical seed mass and its size. The proposed correlation is roughly consistent only with the results of those two systems. It over predicts the critical seed mass for small-sized seeds and under predicts for large seeds (Y. Tseng et al., 2014). The largest seed size used in their investigations was 200 μm .

Rane et al. (2014) numerically investigated the flow patterns in 11 industrial crystallizers (volume =100 L) through CFD. Further, they coupled the PBM with CFD to obtain accurate results. They found that the CSD obtained from the different crystallizer was varying due to the various flow patterns and turbulence characteristics. Hence the internals of the crystallizer and the flow patterns affect the CSD.

Temmel et al. (2016) reported that crystals bigger than 1 to 1.5 mm could not be investigated due to sedimentation inside the flow-through cell. He also noted that the saturation temperature limit for the device is 35 to 40°C since the cell cannot be tempered and the blockage of the suspension flow can occur.

Most of the published literature concerning CFD modelling of crystallization processes considers population balance equations (PBE) to predict the particle size distribution (PSD) (Öncül et al. 2006; Wan and Ring 2006; Richards 2012). The PBE is often solved in a simplified manner using either the standard Method of Moments (MOM) or a Quadrature Method of Moments (QMOM, DQMOM and derived formulations), providing an alternative to MOM for size-dependent growth, aggregation and breakage.

It is also observed that the liquid volume of 24L is advantageous compared with a larger liquid volume of 35L of the crystallizer (Ashraf Ali et al., 2015). Hence in the current work, 24L crystallizer volume is considered. The optimized parameters (seed crystal size : 0.5 mm; injection location of crystal: above the stationary baffle) from the previous study are followed (Ashraf Ali et al. 2015).

Further, Temmel et al. (2016) experimentally found optimum kinetic parameters by considering KH_2PO_4 crystals in water for a 24 L crystallizer. Lewis et al. (2015) predicted CSD using known kinetic models by integrating the population balance equation (PBE) into the CFD solver. Still, the spatial inhomogeneity in temperature distribution, supersaturation and solid concentration are not considered in their lumped parameter methodology. These parameters significantly influence the scaleup of the crystallizer.

CHAPTER 2

SCOPE AND OBJECTIVES OF THE WORK

2.1 Scope

In a stirred vessel, the energy dissipation is high with local gradients; various impellers and baffles produce different flow patterns and mixing. The hydrodynamics of a given system influences scaleup in the crystallization process. Hence, the optimum configuration for the crystallization process is crucial to obtain the desired CSD.

Thus, in the present work, the flow field and mixing in the stirred vessel is numerically investigated using CFD. The effect of the draft tube baffle on the suspension characteristics of solid particles is investigated. Further, CSD, nucleation and growth rates of KDP crystals are predicted by incorporating solubility, crystal growth and nucleation kinetics through coupled CFD-PBE approach in the stirred vessel. The performance of the crystallization process in the stirred vessel system is improved by introducing baffle configuration. The influence of the amount of seed, seed crystal size and temperature on CSD is investigated.

2.2 Objectives

The objectives of the present work are:

1. To find an optimum impeller speed in batch stirred vessel.
2. To find a suitable draft tube baffle configuration that supports liquid circulation, and mixing for a single phase.
3. To find the significance of the baffles for multiphase system using Poincare maps and Shannon entropy through the Euler-Lagrangian method and solid suspension characteristics using Euler-granular method.
4. To predict the desired crystal size distribution (CSD) using the population balance model (PBM).
5. To study the effect of seeding temperature, mass and size on the CSD.

2.3 Organization of the thesis

Chapter 1: Overview of the literature on hydrodynamics, mixing, sedimentation of solids and crystallization

Chapter 2: Objectives of the research work with the research gap

Chapter 3: Results and discussion (flow field and mixing)

Chapter 4: Results and discussion (solid suspension characteristics)

Chapter 5: Results and discussion (nucleation, crystal growth and CSD)

Chapter 6: Summary and conclusion

CHAPTER 3

HYDRODYNAMICS AND MIXING IN A BATCH STIRRED VESSEL

3.1 Introduction

In chemical industries, many of the processes involve multiphase flows. The batch stirred vessels are widely used in industrial applications because they are simple and easy to operate. The stirred vessels are modelled with the assumption of homogenous and uniform properties thorough the vessel (Wan et al. 2005). This assumption does not hold good since there will be inhomogeneity in the vessel, and it strongly depends on the hydrodynamics of the vessel. The performance of the batch stirred vessel is analysed through a flow field, turbulence characteristics, circulation rate, homogeneity and solid distribution (Ochieng and Onyango 2010).

Ashraf Ali et al. (2013) analysed the performance of a batch stirred vessel numerically through CFD. They used the standard k- ϵ model to characterise the liquid-phase turbulence. Bakker and Fasano (1998a) analysed mixing time in the stirred vessel and found that the performance of the system is affected when the process occurs at a smaller time scales than the mixing time scale. Hence, to design a batch stirred vessel, a mixing timescale is needed to be identified. Baldyga and Bourne (1984b) and Meroney and Colorado (2009) used baffles in the stirred vessel to determine the mixing time scale, dead zones in high aspect ratio tanks.

In the present section, draft tube baffles are introduced in the stirred vessels to overcome the solid sedimentation. The hydrodynamics of the draft tube baffled system is investigated to find an optimum rotational speed of an impeller. Then, to improve the flow field, various geometric modifications are incorporated. These predictions are further verified by analysing liquid circulation and mixing.

3.2 Methodology

3.2.1 Geometry of the batch stirred vessel

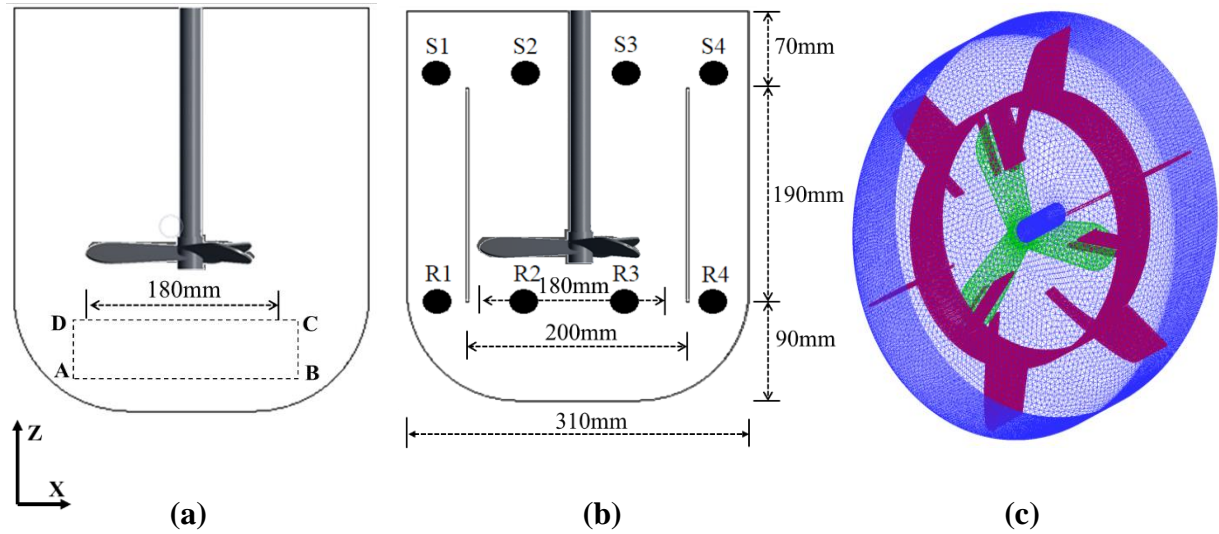


Figure 3.1 Schematic representation of the (a) unbaffled (b) baffled (c) 3D mesh for the baffled stirred vessel.

The schematic of the stirred vessel is shown in Figure 3.1. The batch stirred vessel has an inner diameter of 310 mm with a vertical height of 350 mm with a total capacity of 24 L. The impeller is placed at the centre of the stirred vessel, and it has three blades diameter of 180 mm as shown in Figure 3.1(a). These impeller blades are pitched horizontally at an angle of 30° . The width of the impeller blade near the hub is 22mm and the tip of the blade is having a radius of 23 mm. The impeller shaft is having a diameter of 22 mm with the hub height of 28 mm. The impeller is placed at the height of 90 mm from the bottom of the vessel. The rectangular box ABCD below the impeller region in Figure 3.1 (a) is used to calculate the liquid circulation in the stirred vessels.

The geometry and the dimensions of the baffled stirred vessel is taken from the Max Planck Institute research group [The Laboratory of Fluid Dynamics and Technical Flows] (Ashraf Ali et al. 2013), Magdeburg Germany. The Figure 3.1(b) is the schematic of the baffled stirred vessel. In the baffled stirred vessel, the draft tube is placed at the height of 90 mm from the vessel bottom, and its height is 190 mm with 200 mm inner diameter. This draft tube (vertical lines in Figure 3.1(b)) consists of flat baffles of 50 mm and is arranged radially. The internal baffles are composed of three

rectangular blades arranged at an angle of 120° and the six outer blades arranged at an angle of 60°.

The Figure 3.1(c) shows the surface mesh of the baffled stirred vessel. The blue colour is the surface mesh for the impeller shaft, with green colour indicating the impeller blades and magenta colour for the draft tube baffle.

3.2.2 CFD modelling

The hydrodynamics in batch stirred vessel is numerically investigated at a fixed fluid temperature of 25°C (iso-thermal). The modified version of the Reynolds number is used to find the nature of the flow field in the stirred vessel (Galletti et al. 2004; Ashraf Ali et al. 2013). This is calculated by

$$Re = \frac{ND^2\rho}{\mu} \quad (3.1)$$

Where, N is the speed of the impeller and D is the diameter of the impeller. The water properties ($\rho = 998.4 \text{ kg/m}^3$; $\mu = 0.01003 \text{ Pa. s}$) is used to analyse the flow field. The calculated Re for the impeller speeds (50 to 350 rpm) is in the range of 90,560 to 241,500. Hence, the flow field is described using a turbulence model.

The flow field is governed by continuity and momentum equations (Marshall and Bakker 2003; Ashraf Ali et al. 2013). The equation of continuity is given by

$$\frac{\partial}{\partial x_i}(u_i) = 0 \quad (3.2)$$

Here u_i represents the i^{th} component of fluid velocity. The Reynolds time-averaged Navier Stokes equation is given by

$$\rho \frac{\partial(u_i)}{\partial t} + \rho \frac{\partial}{\partial x_j}(u_i u_j) = \frac{-\partial p}{\partial x_i} + \frac{\partial}{\partial x} \left[\mu \left(\frac{\partial u_i}{\partial x_i} + \frac{\partial u_j}{\partial x_i} - \frac{2}{3} \frac{\partial u_k}{\partial x_k} \delta_{ij} \right) \right] + \frac{\partial}{\partial x_j} (-\rho \overline{u'_i u'_j}) + \rho g_i + F_i \quad (3.3)$$

The term $\overline{u'_i u'_j}$ denotes Reynolds stress term. Standard k-ε model has been used

extensively to predict accurately the turbulence flow in stirred vessels (Mendoza-Escamilla et al. 2018). These Reynolds stresses introduce additional unknowns to the RANS equations. These are obtained through the Boussinesq hypothesis:

$$-\rho \overline{u'_i u'_j} = \frac{2}{3} \rho k \delta_{ij} + \left[\mu_t \left(\frac{\partial u_i}{\partial x_j} + \frac{\partial u_j}{\partial x_i} \right) \right] \quad (3.4)$$

Here, μ_t is the turbulent viscosity, and k is turbulence kinetic energy. This is calculated through velocity fluctuations.

$$k = \frac{1}{2} \left(\overline{u_x'^2} + \overline{u_y'^2} + \overline{u_z'^2} \right) \quad (3.5)$$

In the liquid phase turbulence standard k- ϵ equation, k and ϵ are given by

$$\rho \frac{\partial(k)}{\partial t} + \rho \frac{\partial}{\partial x_j} (u_j k) = \frac{\partial}{\partial x_i} \left(\mu + \frac{\mu_t}{\sigma_k} \right) \frac{\partial k}{\partial x_i} + G_k - \rho \epsilon \quad (3.6)$$

$$\rho \frac{\partial(\epsilon)}{\partial t} + \rho \frac{\partial}{\partial x_j} (u_j \epsilon) = \frac{\partial}{\partial x_i} \left(\mu + \frac{\mu_t}{\sigma_\epsilon} \right) \frac{\partial \epsilon}{\partial x_i} + C_1 \frac{\epsilon}{k} G_k + C_2 \rho \frac{\epsilon^2}{k} \quad (3.7)$$

Here, G_k is the turbulence generation term and it is defined in terms of velocity gradients by

$$G_k = \mu_t \left(\frac{\partial u_i}{\partial x_j} + \frac{\partial u_j}{\partial x_i} \right) \frac{\partial u_j}{\partial x_i} \quad (3.8)$$

The turbulent viscosity is calculated by

$$\mu_t = C_\mu \rho \left(\frac{k^2}{\epsilon} \right) \quad (3.9)$$

The empirical model constants values are $C_\mu = 0.09$, $C_1 = 1.44$, $C_2 = 1.92$, $\sigma_\epsilon = 1.3$ and $\sigma_k = 1.0$ This obtained from literature (Launder and Spalding 1972).

3.2.3 Simulation methodology - single phase

The hydrodynamics in a batch stirred vessel is investigated using commercial software (ANSYS Fluent v2019 R1). Here, the geometry of the system is modelled using an ANSYS design modeller. The CFD simulations are performed for three grid

sizes such as 5,00,000, 7,50,000 and 1,00,000 elements. These grids are tested to establish the independence of the results on the grid chosen. 7,50,000 grids are found to be optimum. The baffle and tank wall are modelled as stationary with no-slip boundary condition (BC). No-slip velocity BC is imposed at the impeller with zero relative velocity. At the top surface of the stirred vessel is specified as symmetry BC. The CFD simulations were performed for three-time step sizes such as 0.01, 0.001 and 0.0001s, and $\Delta t = 0.001s$ is found to be the optimum.

3.3 Results and discussions

At first, the predicted flow field in a batch stirred vessel is discussed. To analyse the flow field, a vertical plane is chosen at $Y = -0.005$ m. The predicted iso-contours of velocity magnitude are analysed at various time instants for 300 rpm. This is shown in Figure 3.2 (a-e). Here the velocity magnitude is zero at $t = 0$, and the magnitude increases when $t > 0$. The highest liquid velocity gradient is observed close to the impeller. The associated contours of the baffled vessel are shown in Figure 3.2 (f-j).

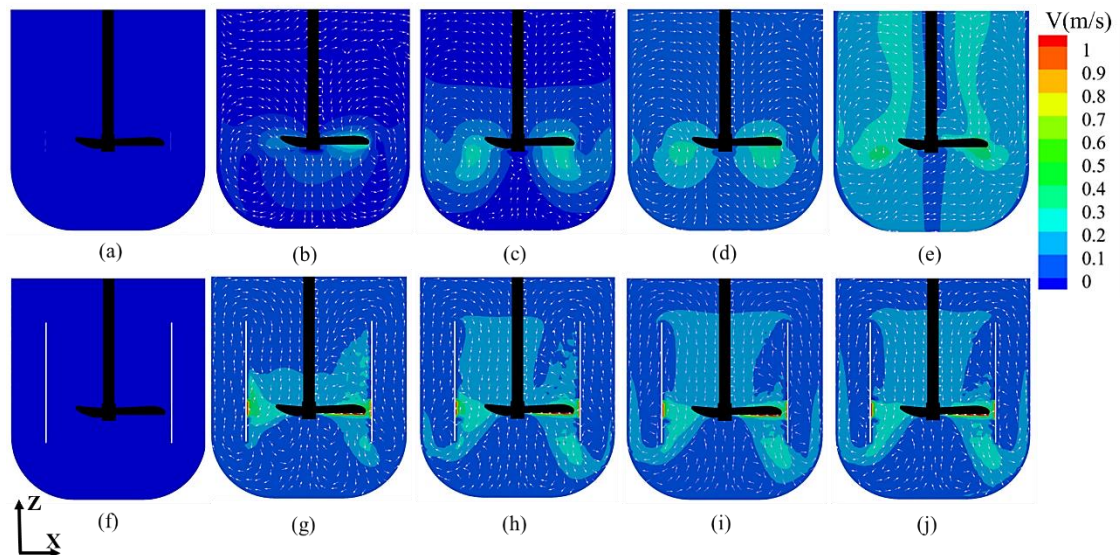


Figure 3.2. Contours of normalised velocity magnitude at different time instants 0s, 0.2s, 0.6s, 1s and 5s for the un baffled (top row) and baffled stirred vessel (bottom row).

It is observed that the velocity magnitude is higher near the impeller in both the un baffled and baffled system. As impeller blades are pitched at an angle of 30 degrees, the liquid is pushed downwards and then forced to move upwards along the vertical

vessel walls. The recirculation in the flow field is observed to be weak in the unbaffled stirred vessel system and strong in the baffled stirred vessel.

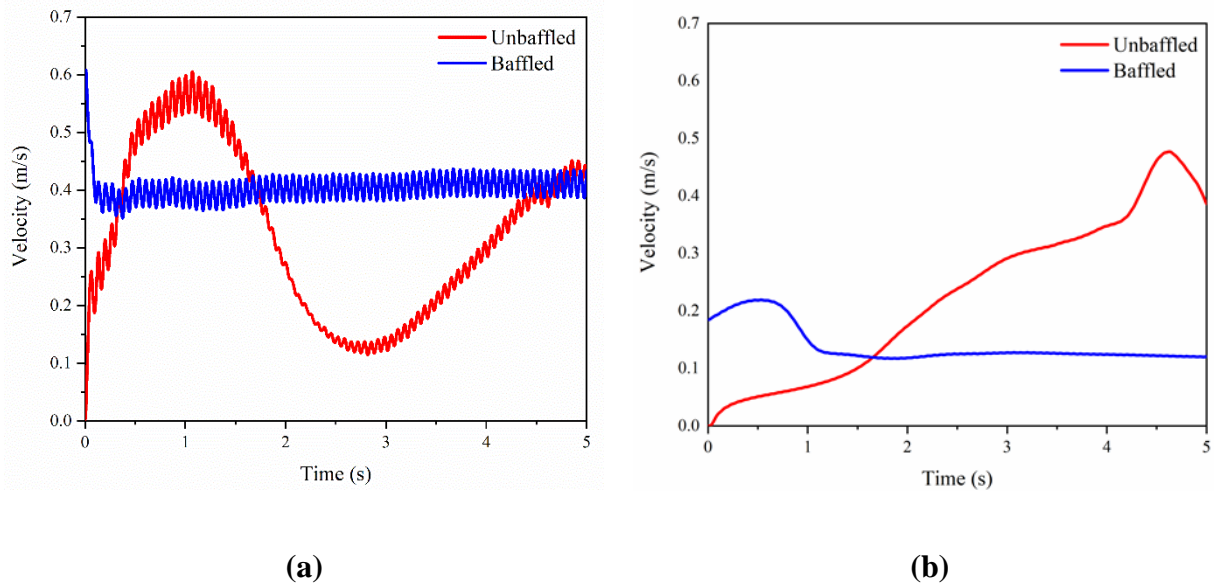


Figure 3.3 Temporal variations of velocity magnitudes at (a) point R and (b) point S

Further, the temporal variation of velocity magnitude at a point is analyzed to quantify the flow field in the unbaffled and baffled vessel. This is shown in Figure 3.3. The velocity magnitude is monitored at points R (near impeller) and S (away from impeller). The periodic oscillations in velocity magnitude are observed near the impeller (point R) due to the rotation of the impeller blades. No velocity oscillations are observed at point S since it is away from the impeller. It is observed that the baffled vessel attains steady flow conditions within 5s of flow time.

The frequency of oscillations presents in the velocity magnitude at point R (near the impeller) is subjected to the power spectral analysis. A dominant frequency of 15 Hz is obtained for 300 rpm. This frequency indicates the rotation of 3 impeller blades at five rps.

To validate the CFD predictions, spatial variation of normalized liquid velocity ($z = -0.005$ m) is compared with available data in literature (Ashraf Ali et al. 2013) and found that the model predictions are consistent.

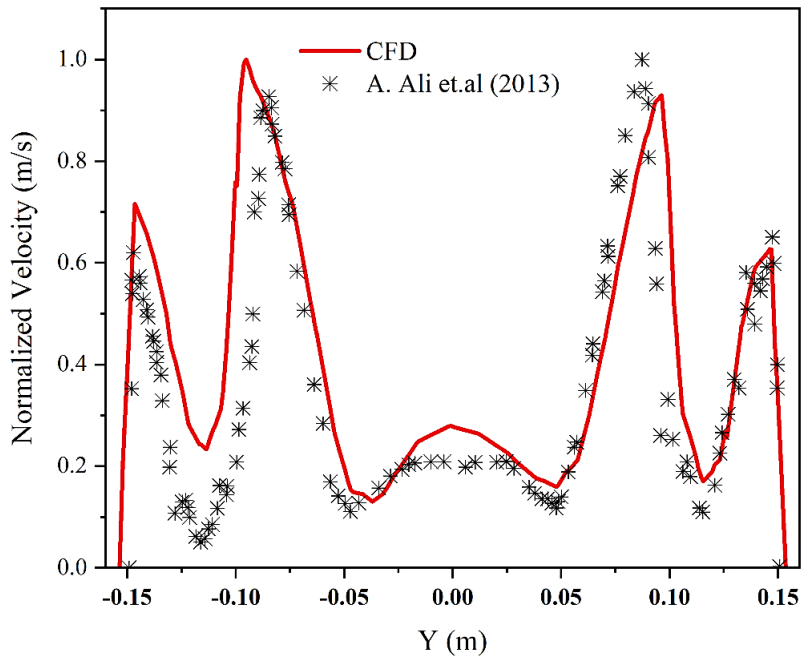


Figure 3.4 Comparison of CFD simulations with literature with normalized velocity magnitude (m/s) along a horizontal line at $z = -0.005$ m

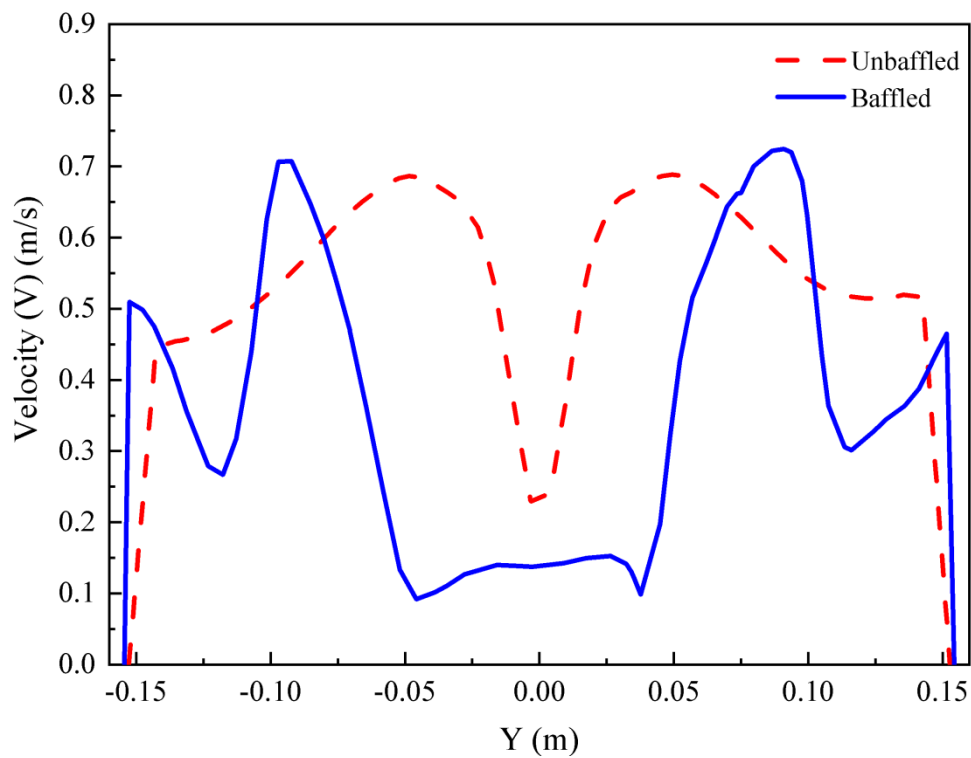


Figure 3.5 Spatial variation of velocity magnitude (m/s) along a horizontal line $z = -0.005$ m

To quantify the flow field further, a horizontal line is chosen below the impeller, and spatial variation of velocity magnitude across the line ($z = -0.005 \text{ m}$) is analyzed. It is observed in Figure 3.5 that the velocity magnitude is zero close to the wall and maximum near the impeller. As impeller speed (300 rpm) in both unbaffled and baffled system is the same, the observed order of magnitude in the velocity is found to be identical for both systems. The nature of the predicted velocity magnitude is attributed to weak recirculation cells below the impeller.

To find an optimum impeller rotational speed in stirred vessel system. The irreversibility induced by the impeller is quantified (liquid circulation). This is calculated by taking the line integral of velocity over a closed region (Fox et al. 2009) using

$$\Gamma = \oint \mathbf{u} \cdot d\mathbf{l} \quad (3.10)$$

Where, ‘ $d\mathbf{l}$ ’ is the small differential element of the closed curve in the flow domain and ‘ \mathbf{u} ’ is the normal liquid velocity. The calculation domain for liquid circulation ABCD is shown in Figure 3.1 (a). The liquid circulation is calculated for various rotational speed of the impeller. The performance of the unbaffled system is compared with a baffled system [Figure 3.6(a)].

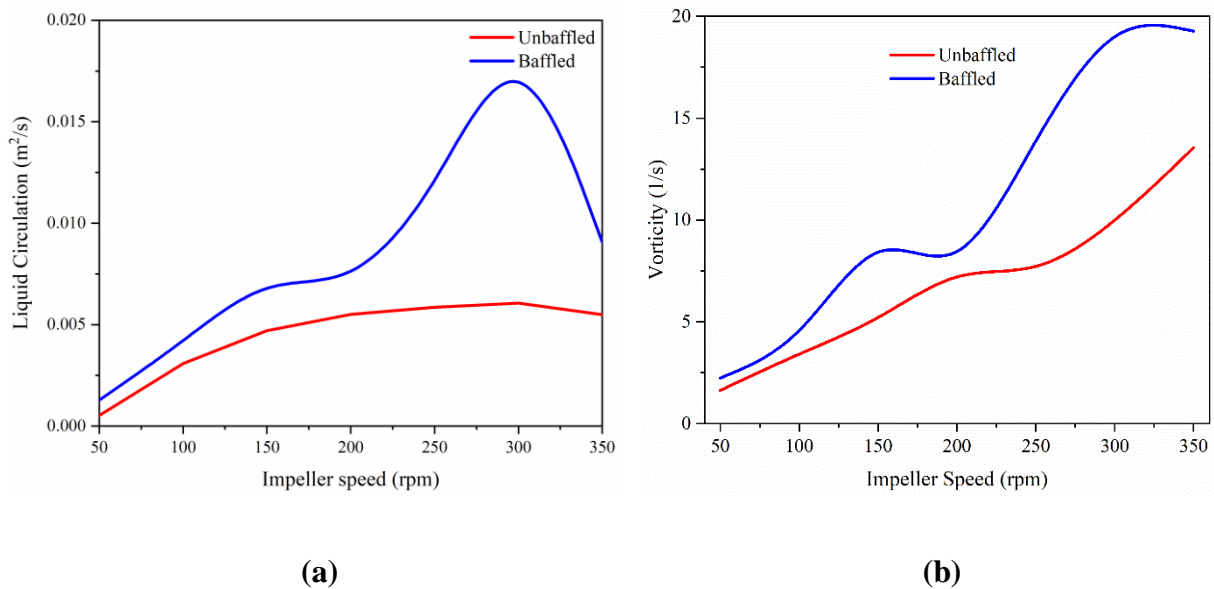


Figure 3.6 Effect of impeller speed on the (a) liquid circulation and (b) vorticity

The calculated liquid circulation in the baffled system is found to be one order of magnitude higher than the unbaffled system at 300 rpm. The liquid circulation is found to be maximum at 300 rpm, and it decreases beyond 300rpm. This is due to a change in the recirculation flow pattern. To verify this optimum impeller speed further, vorticity magnitude is analyzed for baffled and unbaffled system [Figure 3.6(b)]

The vorticity magnitude is observed to be increasing with an increase in rotational motion of the impeller, and its value is high when a baffled system is used. The vorticity magnitude is found to be maximum at 300 rpm. Once again, it confirms the earlier finding of optimum impeller motion (300 rpm).

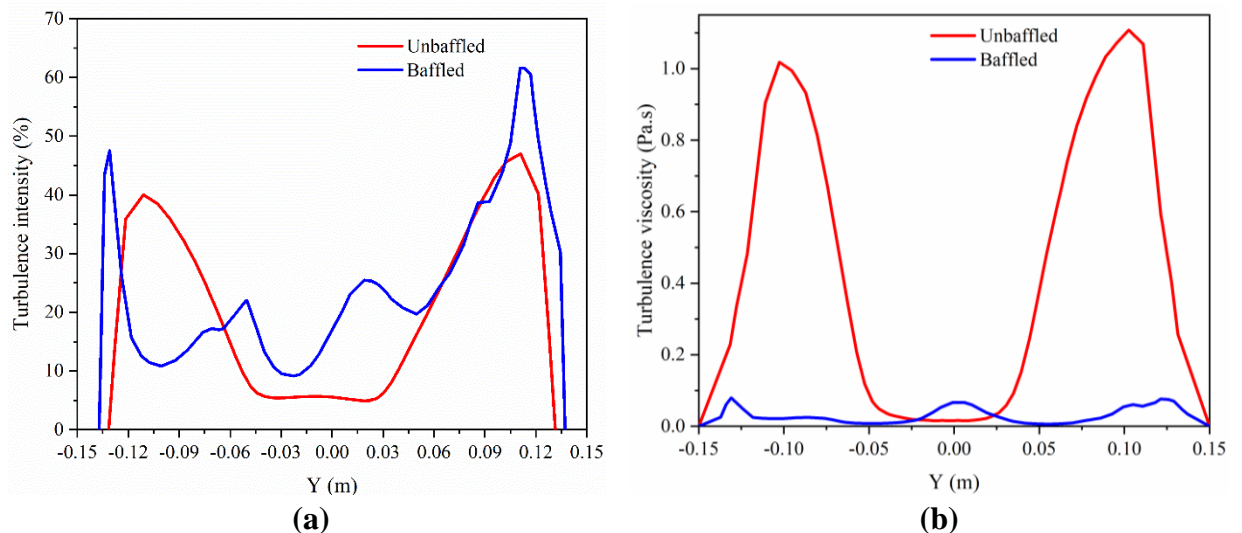


Figure 3.7 (a) Spatial variation of turbulence viscosity (Pa.s) and (b) turbulence intensity (%) along a horizontal line $z = -0.05$ m

To find an optimum system that supports mixing and to carry out the multiphase process, turbulence intensity is analysed along the horizontal line ($z = -0.05$ m) below the impeller. This is shown in Figure 3.7(a). It is observed that the time-averaged magnitude of turbulence intensity (RMS velocity /average velocity) is found to be 12% higher in the baffled system than the unbaffled stirred vessel system. Thus, the baffled system is significantly influencing turbulent flow characteristics and hence the level of turbulence. Further, predicted turbulent viscosity for the same horizontal line ($z = -0.05$ m) is analysed, and it is shown in Figure 3.7(b). It is observed that the magnitude of turbulence viscosity is observed to be low (volume-weighted average: 0.049) in the baffled stirred vessel system in compare with the unbaffled system (volume-weighted

average: 0.386). Thus, the baffled system supports the adequate mixing of fluid elements.

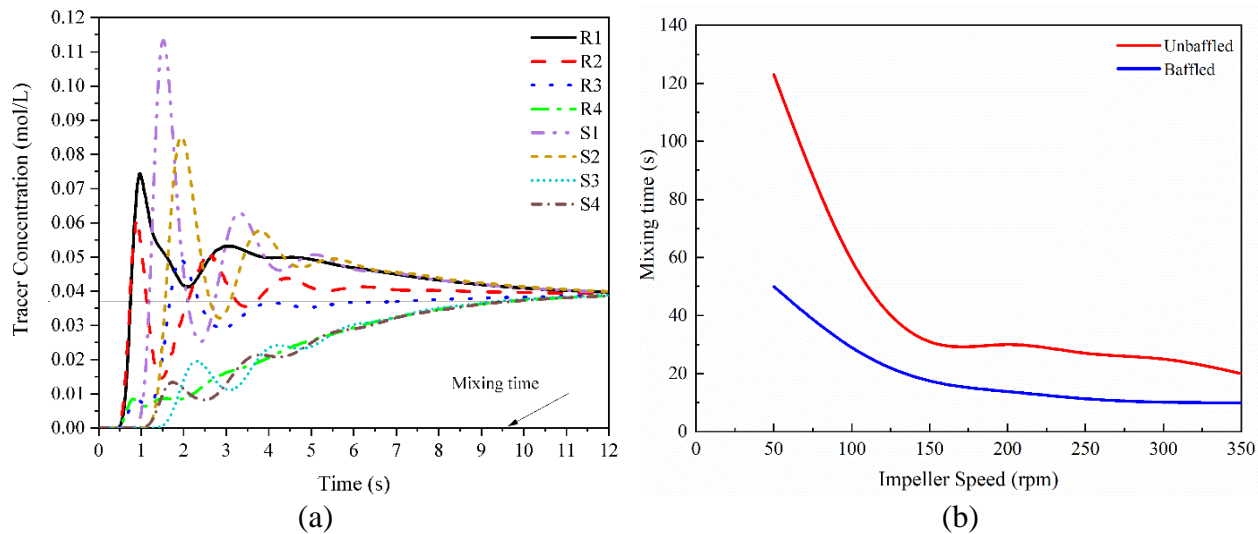


Figure 3.8 (a) Evolution of tracer concentration with time (b) Effect of impeller speed on mixing time

To characterise macro mixing in the stirred vessel system, a pulse of tracer ($c = 55.4 \text{ kmol/L}$) is injected at time $t = 0 \text{ s}$. To quantify the macro-mixing time in the system, eight different point locations [Figure 3.1(b)] are chosen so that four injection locations are above the impeller and the rest are below the impeller. The concentration of tracer is monitored with time, and it is shown in Figure 3.8(a). It is observed that the average concentration of tracer reaches a steady-state value (10 s) after initial transient fluctuations. Here, the time taken for the concentration of tracer to reach 95% of the final concentration is considered to be the macro mixing time (Marshall and Bakker 2003). The mixing time is calculated for various impeller speeds (50 to 350 rpm) for un baffled and baffled stirred vessel, and it is depicted in Figure 3.8(b). The magnitude of mixing time is observed to be smaller for baffled and larger for un baffled stirred vessel system. This is attributed to the significant exchange of mass, momentum between inner (rotating) and outer (stagnant) domain in baffled stirred vessel configuration. Mixing time is found to be constant beyond 300 rpm. This is due to the extent of the convective flow pattern at the higher rotational motion of the impeller. Hence, the impeller speed of 300 rpm is considered optimum.

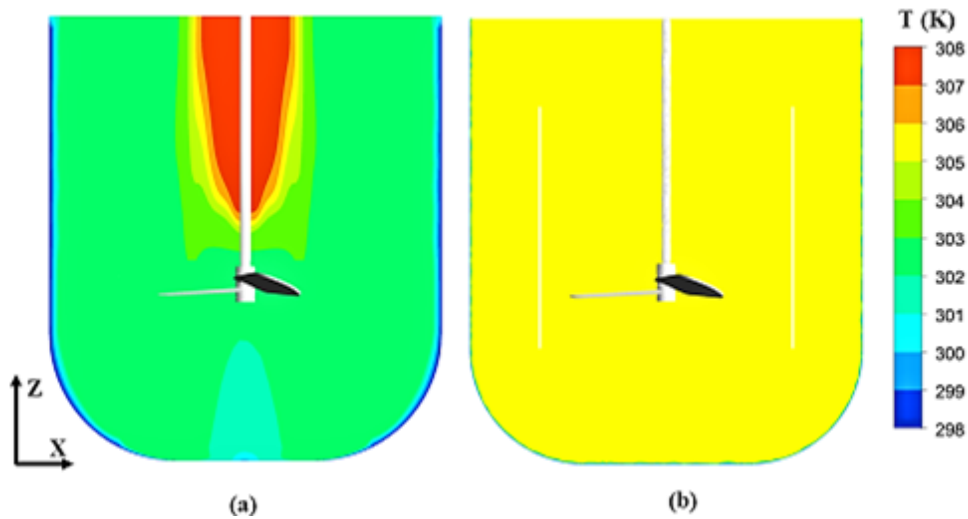


Figure 3.9 Contours of temperature distribution (a) un baffled and (b) baffled stirred vessel

To further analyze the macro mixing characteristics, the water in the stirred vessel is cooled from 308 K by maintaining the walls at a fixed temperature of 298 K. The predicted contours of temperature distribution ($y = -0.005$ m) at 60 s in the un baffled and baffled configuration are shown in Figure 3.9. It is observed that the temperature distribution is uniform in the baffled stirred vessel system and non-uniform in the un baffled system.

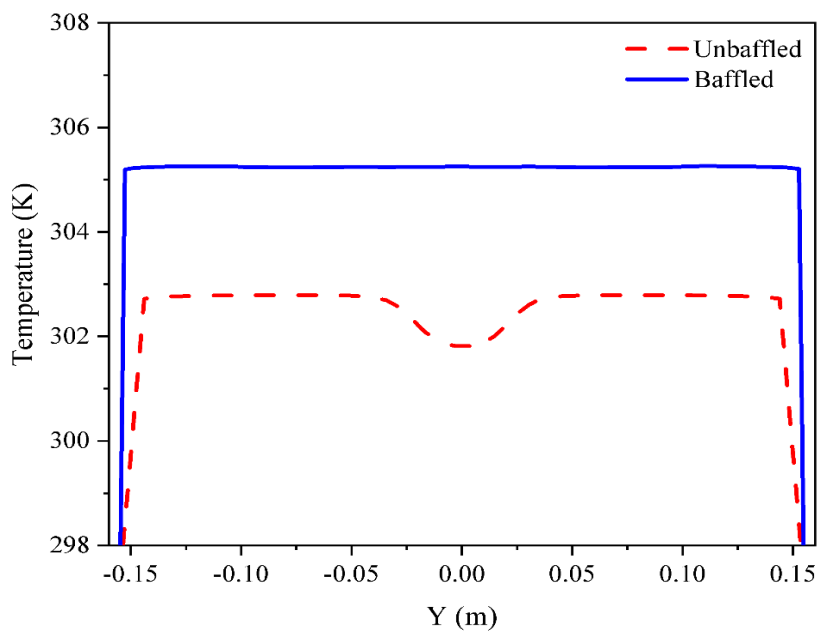


Figure 3.10 Spatial variation of water temperature along $z = -0.005$ m.

To quantify this, a horizontal line is chosen at $z = -0.005$ m, and the spatial variation of temperature of the water is analysed. This is shown in Figure 3.10. It is observed that the temperature is uniform (305 K) for baffled and non-uniform for unbaffled stirred vessel system. This is attributed to weak recirculation in the unbaffled stirred vessel. Thus, the baffled configuration with better thermal homogeneity is found to be more advantageous in batch stirred vessels.

To improve the flow field in the baffled stirred vessel system, various geometric modifications such as impeller blade angle, number of impellers, number of inner baffles and the draft tube baffles are considered.

Table 3.1 Effect of impeller blade angle on the liquid circulation, mixing time and power

Blade angle, (θ)	Avg. Velocity, (m/s)	Liquid Circulation (m^2/s)	Mixing time, (s)	Power, (W)
30°	0.281	0.0203	9	26.5
45°	0.407	0.0122	11	71.7
60°	0.444	0.0027	13	118.3

Here transient 3D CFD simulations are performed at 300 rpm. The effect of the impeller blade angle on the liquid circulation, mixing, and power requirement is reported in Table 3.1. The liquid circulation is found to decrease when the angle of the impeller blade changes from 30° to 60°. The mixing time and power required are found to be the lowest for the impeller blade angle of 30°.

Table 3.2 Effect of the multiple impellers on liquid circulation, mixing time and power

Impellers, (#)	Avg. Velocity, (m/s)	Liquid Circulation (m^2/s)	Mixing time, (s)	Power, (W)
Single	0.281	0.0203	9	26.5
Dual	0.370	0.0067	8	46.2
Triple	0.396	0.0076	8	54.9

The effect of multiple impellers on the liquid circulation and mixing is investigated and reported in Table 3.2. It is observed that a single impeller configuration has the maximum liquid circulation with minimum power requirement.

Further liquid circulation and mixing are investigated by varying the number of inner baffles and depicted in Table 3.3. The liquid circulation is found maximum when the numbers of inner baffles are three. It is observed that the number of inner baffles does not affect the macro-mixing time because the inner baffles improve the mixing only in the draft tube region. It is also observed that the power requirement increases with the increase of the inner baffles

Table 3.3 Effect of the number of inner baffles on the liquid circulation, mixing time and power requirement

Inner baffle, (#)	Avg. Velocity, (m/s)	Liquid Circulation (m²/s)	Mixing time, (s)	Power, (W)
2	0.300	0.0073	9	26.8
3	0.281	0.0203	9	26.4
4	0.290	0.0083	9	27.0
5	0.287	0.0034	9	27.3
6	0.285	0.0022	9	27.4

Further, the geometry with respect to the baffles on the draft tube is considered, the modifications as shown in Figure 3.11. Here, the draft tube with the baffles modifies the flow field and hence the liquid circulation. The ANSYS Design Modeller (v2019 R1) is used to create the internals of the draft tube and the baffles. The details of modifications are reported in Table 3.4, and the schematic front and top views are shown in Figure 3.11.

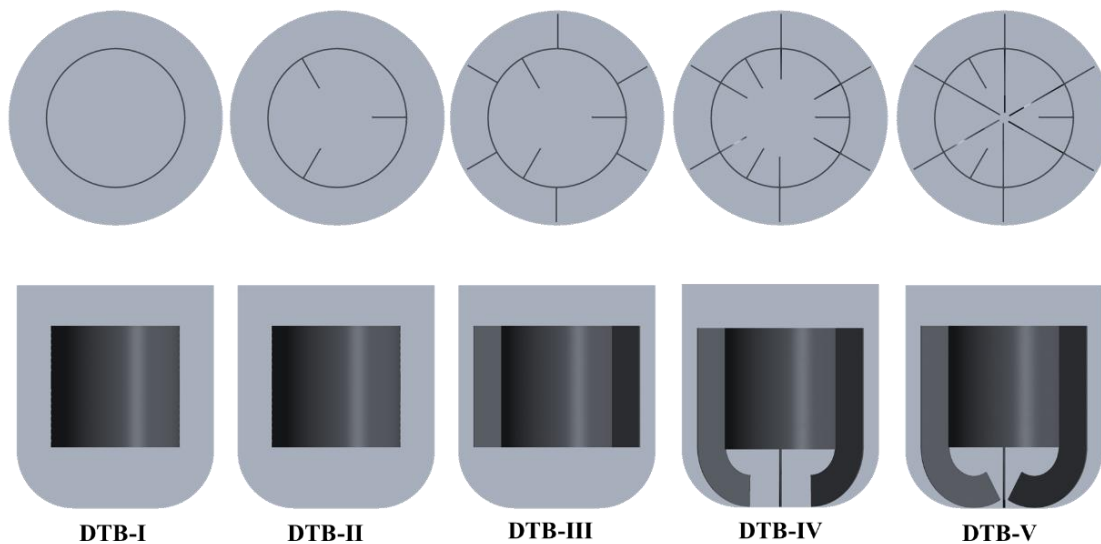


Figure 3.11 Schematic of various draft tube configurations used in the numerical investigation.

Table 3.4 Various draft tube baffle modifications used.

Sl. No	Name	Modifications
1	DTB-I	Draft tube of 200 mm diameter
2	DTB-II	Draft tube of 200 mm diameter with three internal baffles
3	DTB-III	Draft tube of 200 mm diameter with three internal baffles and six external baffles
4	DTB-IV	Draft tube of 200 mm diameter with three internal baffles and six external baffles extending downward with an arc angle of 90°
5	DTB-V	Draft tube of 200 mm diameter with three internal baffles and six external baffles extending downward with an arc angle of 120°

Here transient 3D CFD simulations are performed for the various draft tube systems. The predicted flow field for 300 rpm is shown in Figure 3.12. The inner baffle increases the magnitude of velocity in the agitation zone as well as the region below the impeller. This directs the flow axially.

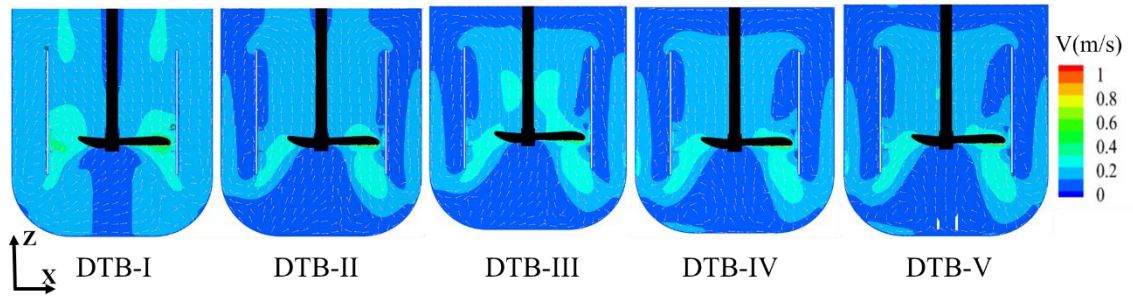


Figure 3.12 Contours of velocity magnitude for various draft tube configurations

Here, the velocity magnitude is observed to be minimum at the bottom of the vessel when only a draft tube (DTB-I, Figure 3.12) is used. The addition of a draft tube with inner baffles (DTB-II, Figure 3.12) directs the flow downward and hence increases the magnitude of velocity. The draft tube baffle with external baffles (DTB-III, Figure 3.12) does not significantly increase the velocity magnitude at the bottom of the vessel. The curved outer draft tube baffles enhance the flow field and hence velocity magnitude at the bottom of the stirred vessel. The outer draft baffle with angle (70° , 90° , 120°) increases (DTB, DTB-IV, DTB-V, Figure 3.12) the flow field and level of turbulence which in turn the velocity magnitude.

Table 3.5 Effect of geometric modification on liquid circulation and mixing time

System type	Liquid Circulation (m^2/s)	Mixing time, (s)
DTB-I	0.0011	11
DTB-II	0.0088	10
DTB-III	0.0071	10
DTB-IV	0.0379	9
DTB-V	0.0249	13

To find suitable draft tube configuration that supports the flow field at the bottom of the vessel, the liquid circulation is calculated for the draft tube systems described above. The area chosen for liquid circulation calculation is the same as mentioned before. This is shown in Table 3.5. The magnitude of liquid circulation is found to be maximum for DTB-IV in comparison with another configuration. This is because the baffle used in DTB-IV directs the flow upwards in the center of the stirred

vessel.

3.4 Summary

The flow field and mixing in a batch stirred vessel system is numerically investigated using CFD. The performance of the unbaffled stirred vessel is improved by incorporating a draft tube baffle. The spatial variation of velocity magnitude is analysed to quantify the flow field. It is found that the recirculatory flow field prevails in the baffled stirred vessel system. The liquid circulation and predicted vorticity magnitude are analysed for various rotational motion of the impeller, and optimum impeller speed (300rpm) is identified. Further, the predicted turbulence parameters are analysed for unbaffled and baffled stirred vessel systems. The magnitude of turbulence intensity is found to be significant in the baffled stirred vessel system. The effect of the flow field on the macro mixing is analysed by injecting a buoyant tracer into the system. The mixing time was found to be less for the baffled stirred vessel system. These predictions are further verified by maintaining the water and wall of the stirred vessel at different temperatures. The temperature distribution is found to be uniform for the baffled stirred vessel system.

Further various baffle configurations are incorporated to enhance the flow field in the batch stirred vessel. The draft tube baffle with three internal baffles and six external baffles of 90° angle (DTB-IV) is more advantageous. The flow field and mixing were analyzed for various impeller and baffle configurations. The mixing time was found to decrease for the addition of each component of the draft tube. The DTB-IV with an impeller speed of 300 rpm is found to be optimum.

CHAPTER 4

SOLID SUSPENSION IN STIRRED VESSELS

4.1 Introduction

Stirred vessels are the commonly used process equipment for solid-liquid systems in industries. The impeller rotation generates turbulence and creates a suspension of solids in the stirred vessels. In a liquid-solid system, solids should remain in complete suspension to achieve high mass transfer rates between the phases (Vedantam and Ranade 2013). However, in reality, the suspension density of the solids strongly is depending on the geometric and operating parameters of the stirred vessel.

The suspension density can be quantified experimentally either by varying the just suspension speed or by modifying the geometry of the system. This cannot be generalised for all the stirred vessels (Ochieng and Onyango 2010). Hence, numerical investigations based on macroscopic models are used to predict suspension density (Sommerfeld and Decker 2004; Visuri et al. 2011), and these models characterise the flow field spatially and temporally (Derksen 2003). Appropriate drag models must be chosen in order to capture the suspension characteristics of the solids.

In most of the published literature, the solid suspension problems are addressed either by modifying the geometry of the stirred vessels or by increasing rotational impeller speed. The cloud height and suspension speed were used to quantify the sedimentation characteristics (Hicks et al. 1997; Oshinowo and Bakker 2001; Bittorf and Kresta 2003; Ochieng and Lewis 2006; Ochieng and Onyango 2010).

To improve the flow field and to support solid suspension, various geometric modifications are incorporated. These predictions are further verified by analysing the sedimentation of solids.

4.2 Methodology

4.2.1 CFD modelling

In order to predict the suspension characteristics in the stirred vessels, two-fluid model is used. When the volume fraction of the solid is less than 10%, the particle dynamics is tracked in a Lagrangian way. Further, the suspension characteristics suspension of solids with volume fraction greater than 10% is predicted using the Euler-granular model.

4.2.1.1 Euler Lagrangian model (DPM)

To compute particle motion in the fluid domain, the momentum balance is applied to the individual particles (Ashraf Ali and Pushpavanam 2011).

$$M_p \frac{du_p}{dt} = \sum F_{ext} \quad (4.1)$$

Here, m_p is the particle mass (kg), u_p is the velocity of the particle (m/s), and $F_{ex,t}$ is the other external forces influencing the particle motion. The particles are assumed to be spherical, and it obeys Stokes Law. The drag coefficient is used to calculate the drag force that is determined using the particle Reynolds number (Srinivasa and Jayanti 2007). The displacement of the particle for each time step, δt , is calculated using forward Euler integration

$$X_i^n = x_i^k + u_{pi} \delta t \quad (4.2)$$

Where “n” refers to the new values, k refers to the old values, and u_{pi} denotes the velocity. In the DPM simulations, the particles are tracked throughout the computational domain.

The particles location is not sufficient enough to analyze the quality of the suspension. Hence the concept of Shannon entropy is used to quantify the spatial distribution of particles in the stirred vessel (Krishnaveni et al. 2017). Here, the horizontal plane is split into regions called bins. Every bin was represented by $j = 1, 2, \dots, M$. Particle size is denoted by “c”, where $c = 1, 2, \dots, M$. The probability distribution of individual particle size in every bin is calculated to characterize Shannon entropy (Madana and Ashraf Ali 2020).

$$S = - \sum_{j=1}^M \sum_{c=1}^c P_{j,c} \ln P_{j,c} \quad (4.3)$$

Here $P_{j,c}$ denotes the joint probability that a particle of size c is located in bin j . It is given by

$$P_{j,c} = \frac{\frac{n_{j,c}}{P_c}}{\sum_{i=1}^M \sum_{c=1}^c \frac{n_{i,c}}{P_c}} \quad (4.4)$$

where, $n_{j,c}$ represents the particles of size c present in bin j . P_c indicates the total count of the particles of size c present in every bin.

The summation of $S_{(location)}$, which represents the entropy of the spatial distribution of particle irrespective of size and $S_{location(particle \ size)}$, indicating the interaction of particles conditional over location, describes the total entropy.

$$S_{(location)} = - \sum_{j=1}^M P_j \ln P_j \quad (4.5)$$

where, the probability P_j indicates that a collection of particles, irrespective of particle size in bin j

$$P_j = \frac{\sum_{c=1}^c \frac{n_{j,c}}{P_c}}{\sum_{i=1}^M \sum_{c=1}^c \frac{n_{i,c}}{P_c}} \quad (4.6)$$

The stirred vessel is divided into several uniform cells called as bins. The probability of the particle distribution is calculated using equation 4.6. The higher the value of the probability and hence the Shannon entropy indicates a better distribution of the solid particles. This indicates the improvement of the suspension quality of the solids in the stirred vessel.

4.2.1.2 Euler Granular Model

The Euler-granular (EG) model uses the kinetic theory of granular flows (KGTf) to predict the behavior of the solid phase, which is different from the liquid phase. In order to predict the solid stresses, an analogy is made between the random particle motion due to particle-particle collisions and the thermal motion of molecules in a gas, considering the inelasticity of the granular phase. The kinetic energy related

to the particle velocity fluctuations is denoted by a granular temperature which is proportional to the mean square of the random motion of solid particles.

This model assumes that an interpenetrating continuum exists between the solid and liquid phase at all the points in space. The liquid is considered as the primary phase, whereas the solid is considered as the secondary or dispersed phase.

The volume of the solid phase V_s is defined as

$$V_s = \int_V \alpha_s dV \quad (4.7)$$

Where the volume fraction of both solid and liquid is given by

$$\alpha_l + \alpha_s = 1 \quad (4.8)$$

The continuity equation for liquid phase (l) and solid phase (s) is represented by

$$\frac{\partial}{\partial t} (\alpha_l \rho_l) + \nabla \cdot (\alpha_l \rho_l \vec{u}_l) = 0 \quad (4.9)$$

$$\frac{\partial}{\partial t} (\alpha_s \rho_s) + \nabla \cdot (\alpha_s \rho_s \vec{u}_s) = \sum (m_{ls} - m_{sl}) \quad (4.10)$$

Where α , ρ , \vec{u}_l and \vec{u}_s are the volume fraction, density and velocity of the liquid and solid phase respectively. The first term is the transient term; the second term is the convective term on the LHS and on the RHS m_{sl} characterizes the mass transfer from the solid to the liquid phase.

The conservation equations are derived by the mixture theory approach (Fluent Theory Guide 2013). Momentum equation for both the phases are written as,

$$\frac{\partial}{\partial t} (\alpha_s \rho_s \vec{u}_s) + \nabla \cdot (\alpha_s \rho_s \vec{u}_s \vec{u}_l) = -\alpha_s \nabla p + \nabla \cdot \bar{\tau}_s + \alpha_s \rho_s g + \sum (\overrightarrow{R_{sl}} - m_{sl} \vec{u}_{ls} - m_{ls} \vec{u}_{sl}) + (F_{lift,s} + F_{td,s}) \quad (4.11)$$

Where p is the pressure, P_s is the solids pressure, $\bar{\tau}$ is the solid stress-strain tensor, $F_{lift,s}$ is the lift force, $F_{td,s}$ is the turbulent dispersion force and R_{ls} is the interaction force between the liquid and solid phases, and the equation must be closed.

$$\bar{\tau}_s = -P_s \bar{I} + \alpha_s \mu_s (\nabla \vec{u}_s + \nabla \vec{u}_s^T) + \alpha_s \left(\lambda_s - \frac{2}{3} \mu_s \right) \nabla \cdot \vec{u}_s \bar{I} \quad (4.12)$$

Here μ_s and λ_s are the solids shear and bulk viscosity, P_s is the solid pressure, \vec{V}_{ls} is the interphase velocity defined as $\dot{m}_{sl} > 0$ (for mass transferred from liquid phase to the solid phase) then the velocity $\vec{u}_{ls} = \vec{u}_s$. Then the equation (4.12) is to be closed with proper expressions for the interphase force \vec{R}_{sl} which depends on the friction, pressure, cohesion and other effects and is subject to the constrain that

$$\vec{R}_{ls} = -\vec{R}_{sl} \text{ and } \vec{R}_{ss} = 0 \quad (4.13)$$

The drag force is the dominating force in comparison to lift and other forces in solid-liquid systems. In ANSYS Fluent 2020R1 theory guide uses a simple interaction term expressed as a function of the phase velocities.

$$R_{ls} = -R_{sl} = K_{ls}(\vec{u}_l - \vec{u}_s) \quad (4.14)$$

Where, K_{ls} is the interphase momentum exchange coefficient and does not include the any contribution due to turbulence. The turbulence interphase momentum exchange is modelled with the turbulent dispersion force term $F_{td,s}$ in the equation 4.11. The turbulent dispersion force arises from averaging the interphase drag term. The turbulent drag is modelled as follows

$$K_{ls}(\dot{u}_l - \dot{u}_s) = K_{ls}(\vec{u}_l - \vec{u}_s) - K_{ls} \vec{v}_{dr} \quad (4.15)$$

The term on the LHS of equation 4.15 is the instantaneous drag, and the first term on the RHS is the momentum exchange between the solid and liquid phase, and it appears in equation 4.14. The second term $K_{ls} \vec{v}_{dr}$ is the turbulent dispersion force and \vec{v}_{dr} is the drift velocity and accounts for the dispersion of the solid phase due to transport by turbulent fluid motion. The effect of turbulence dispersion force accounting interphase turbulence momentum transfer is determined by adding a correction term in the interphase momentum exchange equation as proposed by Simonin (Tamburini et al. 2014). The drift velocity is calculated as follows

$$\vec{v}_{dr} = -D_{ls} \cdot \left(\frac{\nabla \alpha_l}{\alpha_l} - \frac{\nabla \alpha_s}{\alpha_s} \right) \quad (4.16)$$

Where D_{ls} , is the liquid-solid dispersion tensor, and for the mixture turbulence model, the dispersion scalar is equal to the mixture turbulent kinematic viscosity. The liquid-solid exchange coefficient K_{ls} is expressed as

$$K_{ls} = \alpha_s \frac{\rho_s f}{\tau_s} d_s \quad (4.17)$$

Where f the drag function and it is defined based on the different empirical models available, d_s is the particle diameter and τ_s is the particulate relaxation time expressed as

$$\tau_s = \frac{\rho_s d_s^2}{18\mu_l} \quad (4.18)$$

f is including a drag function (C_D) that is based on the relative Reynolds number (Re_s). This drag function (C_D) calculated varies for different correlation available in the literature. Various correlations are available in the literature given by Ergun and Orning (1949), Wen and Yu (1966) (for dilute systems), Syamlal and O'Brien (1989) (used for settling of solids) and Gidaspow (1994). The drag model given by Gidaspow (1994) predicted more accurately compared to other models (Moliner et al. 2019). Hence, in the present work, the Gidaspow model is used to predict the interphase momentum exchange (K_{ls}).

Based on the volume fraction of the fluid the exchange coefficient equation is different. The volume fraction of the solution in the crystallisation process accounts for 80% of the total volume. When $\alpha_l > 0.8$, the interphase exchange coefficient K_{ls} is given by

$$K_{ls} = \frac{3}{4} C_D \frac{\alpha_s \alpha_l \rho_l |\vec{u}_s - \vec{u}_l|}{d_s} \alpha_l^{-2.65} \quad (4.19)$$

$$C_D = \frac{24}{\alpha_l Re_s} [1 + 0.15(\alpha_l Re_s)^{0.687}] \quad (4.20)$$

$$Re_s = \frac{\alpha_l \rho_l d_s |\vec{u}_s - \vec{u}_l|}{\mu_l} \quad (4.21)$$

The solid exchange coefficient K_{ls} has the following expression

$$K_{ls} = \frac{3(1+e_{ls})\left(\frac{\pi}{2} + C_{fr,ls}\frac{\pi^2}{8}\right)\alpha_s \rho_s \alpha_l \rho_l (d_l + d_s)^2 g_{0,ls}}{[2\pi(\rho_l d_l^3 + \rho_s d_s^3)]} |\vec{u}_l - \vec{u}_s| \quad (4.22)$$

Where e_s = the restitution coefficient, $C_{fr,ls}$ = the coefficient of friction between the solid phase particles, d_l = particle diameter of the solid l and $g_{0,ls}$ is the radial distribution coefficient

For granular flows, i.e., where the solids volume fraction is less than its maximum allowed value, a solids pressure is calculated independently and used for the pressure gradient term ∇p in equation 4.11. The pressure exerted on the containing wall due to the presence of particles. It is the measure of the momentum transfer due to the streaming motion of the particles and collision. The solid Pressure is given by Ma and Ahmadi (1990)

$$P_s = \alpha_s \rho_s \theta_s \left[(1 + 4 \alpha_s g_{0,ss}) + \frac{1}{2} (1 + e_s)(1 - e_s + 2\mu_{fr}) \right] \quad (4.23)$$

Where, θ_s is the granular temperature and μ_{fr} is the frictional viscosity. The frictional viscosity (μ_{fr}) is applicable for the packing limit is greater than 0.63. The Granular temperature θ_s for the solid phase is proportional to the kinetic energy of the random motion of the particles and it is defined as the average of the square of the fluctuating particle velocities \vec{C}_s

$$\theta_s = \frac{1}{3} \overline{C_s^2} \quad (4.24)$$

$$\vec{C}_s = \vec{v}_s - \vec{u}_s \quad (4.25)$$

Where, \vec{V}_s is the ensemble average particle's random velocity within a finite volume and time interval. The granular temperature is obtained by solving its transport equation in the algebraic form, neglecting the convection and diffusion terms

$$\frac{3}{2} \left[\frac{\partial(\alpha_s \rho_s \theta_s)}{\partial t} + \nabla \cdot (\alpha_s \rho_s \vec{u}_s \theta_s) \right] = \phi_{ls} - \gamma_s \quad (4.26)$$

The transfer of kinetic energy of random fluctuations is expressed as

$$\phi_{ls} = -3 K_{ls} \theta_s \quad (4.27)$$

Collisional energy dissipation for the solids is given by Lun et al. (1984):

$$\gamma_s = \frac{12(1-e_s^2)g_{0,ss}}{d_s\sqrt{\pi}} \rho_s \alpha_s^2 \theta_s^{3/2} \quad (4.28)$$

The radial distribution function for the solids $g_0(\alpha_s)$ is a correction factor that modifies the probability of the particle collisions between particles when the granular phase becomes dense. The radial distribution is given by Gidaspow for a single solid phase:

$$g_{0,ss} = \left(1 - \left(\frac{\alpha_s}{\alpha_{s,max}}\right)^{1/3}\right)^{-1} \quad (4.29)$$

The solid stress tensor in equation 4.12 contains shear and bulk viscosities. Shear viscosity occurs due to kinetic motion and collision interaction of particles. The total solid-phase viscosity (μ_s) is the sum of collisional ($\mu_{s,col}$), kinetic ($\mu_{s,kin}$), and frictional terms ($\mu_{s,fr}$).

$$\mu_s = \mu_{s,col} + \mu_{s,kin} + \mu_{s,fr} \quad (4.30)$$

The third term in equation 4.30 is only considered when the solid volume fraction is greater than the frictional packing limit. The first term of equation 4.30 is given by Gidaspow et al. (1992), and the second term is given by Gidaspow et al. (1989)

$$\mu_{s,col} = \frac{4}{5} \alpha_s \rho_s d_s g_{0,ss} (1 + e_s) \left(\frac{\theta_s}{\pi}\right)^{1/2} \quad (4.31)$$

$$\mu_{s,kin} = \frac{10 \rho_s d_s \sqrt{\theta_s \pi}}{96 \alpha_s (1 + e_s) g_{0,ss}} \left[1 + \frac{4}{5} g_{0,ss} \alpha_s (1 + e_s)\right]^2 \quad (4.32)$$

Solid bulk viscosity accounts for particle resistance to expansion and compression given by λ_s (Lun et al. 1984)

$$\lambda_s = \frac{4}{3} \alpha_s^2 \rho_s d_s g_{0,ss} (1 + e_s) \left(\frac{\theta_s}{\pi}\right)^{\frac{1}{2}} \quad (4.33)$$

Turbulence in the system is accounted via a dispersed k- ϵ turbulence model, which is a modification of the single-phase k- ϵ model, adapted for liquid-solid

interactions

$$\frac{\partial}{\partial t}(\alpha_l k_l) + \nabla \cdot (\vec{u}_l \alpha_l k_l) = \nabla \cdot \left(\alpha_l \left(\mu_l + \frac{\mu_{t,l}}{\sigma_k} \right) \nabla k_l \right) + \alpha_l G_{k,l} \pm \alpha_l \varepsilon + \alpha_l \pi_{kl} \quad (4.34)$$

$$\frac{\partial}{\partial t}(\alpha_l \varepsilon_l) + \nabla \cdot (\vec{u}_l \alpha_l \varepsilon_l) = \nabla \cdot \left(\alpha_l \left(\mu_l + \frac{\mu_{t,l}}{\sigma_\varepsilon} \right) \nabla \varepsilon_l \right) + \alpha_l \frac{\varepsilon_l}{k_l} [C_{1\varepsilon} G_{k,l} - C_{2\varepsilon} \varepsilon_l] + \alpha_l \pi_{\varepsilon l} \quad (4.35)$$

The term $G_{k,l}$ is the turbulence kinetic energy production due to mean velocity gradient. The turbulence quantities for the solid phase are not obtained from the transport equations. The time and length scales are used to evaluate the dispersion and correlation coefficients, and the kinetic energy of the solid phase.

4.2.2 Simulation methodology – multiphase flow

The quality of the solid suspension in a batch stirred vessel is numerically investigated using commercial software (ANSYS Fluent v2019 R1). The Eulerian - Lagrangian CFD model is used to predict the motion of the solid particles. Here, the CFD simulations are performed using the Discrete Phase Model (DPM) with 50,000 spherical particles of different sizes. These were injected uniformly in a region close to the top of the vessel. The effect of the continuous phase on the dispersed phase is computed through two-way coupling. The discrete Random Walk model is used to obtain trajectories of solids. Poincaré map is generated using the particle information obtained from the DPM simulations. These maps help to visualize the flow structure of the particles on the flow domain.

Further, to analyze the suspension quality for high solid concentrations i.e., the volume fraction ($\alpha > 10\%$) the Eulerian - Granular model is used. Once the steady flow is obtained, 2000 gm of the solids (0.5 mm diameter and 2340 kg/m³ density) are introduced at the bottom of the vessel. The interactions of the solids are predicted through the Gidaspow drag model. The cloud height is calculated to quantify suspension quality in the vessel.

The baffle and tank wall are modelled as stationary with no-slip boundary condition (BC). No-slip velocity BC is imposed at the impeller with zero relative

velocity. At the top surface of the stirred vessel is specified as symmetry BC. The CFD simulations were performed for three-time step sizes such as 0.01, 0.001 and 0.0001s, and 0.001s is found to be the optimum. Here transient CFD simulations are performed with $\Delta t = 0.001s$.

4.3 Results and discussion

To investigate the quality of suspension, solids are injected at the top of the vessel. 10,000 spherical particles of size $500 \mu m$ having the density same as that of the fluid (1000 kg/m^3) are injected into the flow domain. Since the density difference between the particle and fluid is negligible, the influence of drag on the particles on the liquid phase can be neglected.

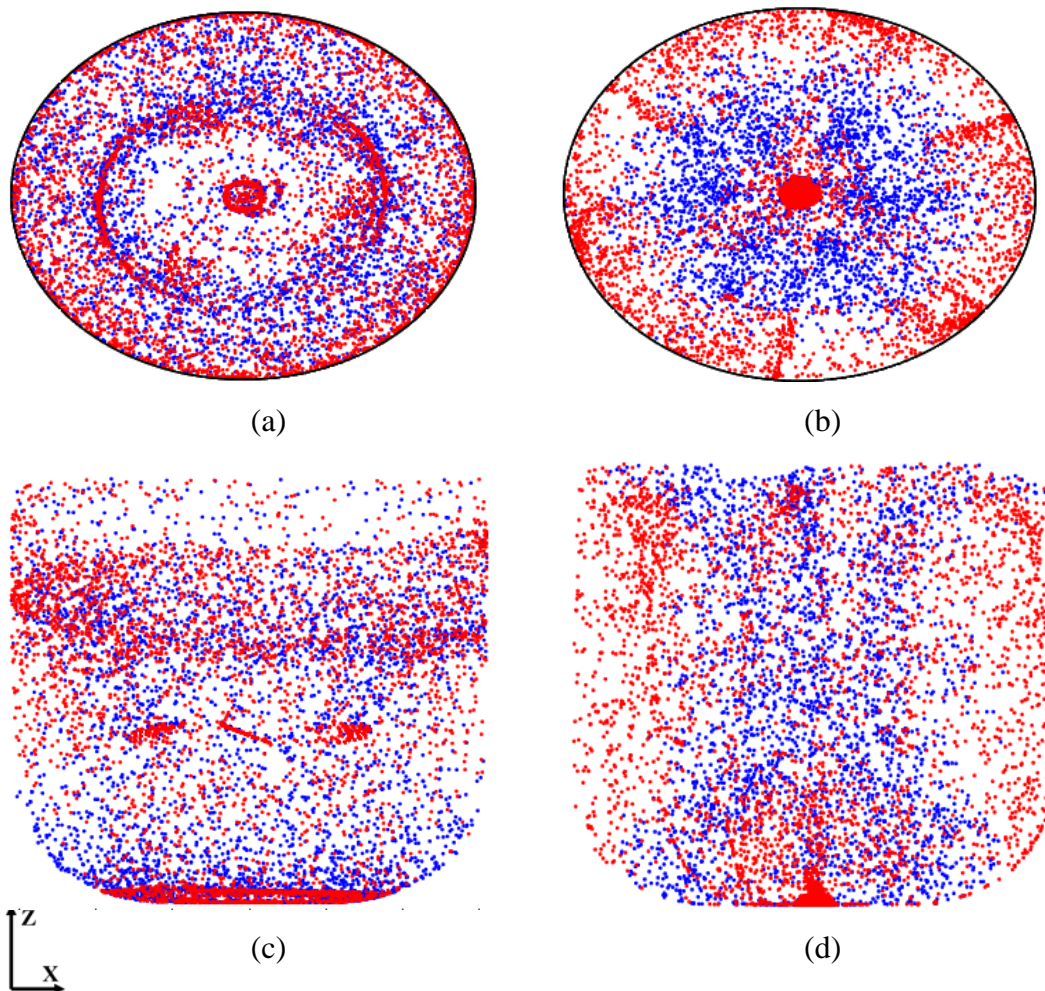


Figure 4.1 Poincaré map for un baffled (a) top view, (b) front view and baffled system (c) top view, (d) front view

Poincaré map is generated using the particle information obtained from the DPM simulations. These maps help to visualize the flow structure of the particles on the flow domain. The Poincaré map for the unbaffled and baffled stirred vessel is shown in Figure 4.1. It is observed in Figure 4.1(a) and (c) that there are uniform circulatory chaotic regions in the unbaffled stirred vessel. The presence of these regions indicate that the mixing is not proper in these regions due to the circulatory flow. When the geometry is modified by introducing the draft tube baffle in the stirred vessel, the position of the particles disintegrates in the Poincaré map and the uniform chaotic region diverges as observed in Figure 4.1(b). Hence, the particle in the baffled stirred vessel are characterized by non-uniform and highly chaotic regions enhancing the mixing of particles in the stirred vessel. The blue colour indicates particle flow downwards and red indicated particle flow in the upward direction as observed in Figure 4.1(c) and (d).

The Poincaré maps give only qualitative information of particle distribution in the stirred vessels. The particle information can be used to quantify the degree of distribution of particles by calculating Shannon entropy (Krishnaveni et al., 2017). The Shannon entropy is calculated the reported in Table 4.1. The uniformity is calculated as

$$U = \frac{e^S}{N} \quad (4.36)$$

Where U is the particle uniformity, S denotes Shannon entropy, and N is the total number of bins used to calculate the Shannon entropy

Table 4.1 Shannon entropy and the uniformity in the stirred vessel

Sl. No	Geometry	Shannon entropy	Uniformity
1	Unbaffled	5.2634	0.135
2	Baffled	7.0547	0.809

The volume of the stirred vessel is divided into 2000 bins. The Shannon entropy is calculated, and it is found that its magnitude is more (relatively good mixing) in the

baffled stirred vessel and minimum (poor mixing) in the unbaffled stirred vessel. The high value of Shannon entropy signifies the degree of uniform distribution of particles across the height of the stirred vessel.

The role of the draft tube and the significance of the baffles on the solid suspension was numerically investigated. The Poincaré maps for the different geometric modifications are shown in Figure 4.2. Since flow field in a stirred vessel is found to be recirculatory in nature. The Poincaré maps are found to be the same for all geometric modifications. Thus, the Shannon's entropy is used to quantify the particle distribution for various baffle configurations.

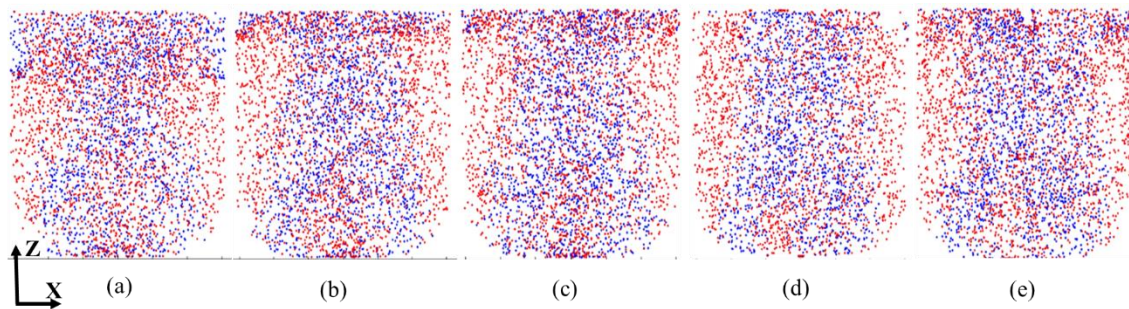


Figure 4.2 Poincaré maps for different geometric modifications (a) DTB-I, (b) DTB-II, (c) DTB-III, (d) DTB-IV and (e) DTB-V

The Shannon's entropy and uniformity of the particles is calculated for the different geometric modifications. This is shown in Table 4.2. The Shannon entropy for DTB-IV is maximum indicating better suspension quality in comparison to the other baffled configurations supporting the findings of hydrodynamics and mixing of the previous section.

Table 4.2 Shannon entropy and the uniformity in the stirred vessel

Sl. No	Geometry	Shannon's entropy	Uniformity
1	DTB-I	6.969	0.743
2	DTB-II	6.995	0.763
3	DTB-III	7.001	0.770
4	DTB-IV	7.054	0.809

Sl. No	Geometry	Shannon's entropy	Uniformity
5	DTB-V	6.969	0.743

The DTB-IV geometry is investigated further by introducing crystals of different densities in the range of 1300 – 2750 kg/m³. Since the densities of the crystal are greater than that of the fluid, the drag law is applicable. Hence 10,000 crystals of 500 μm particle diameter are introduced at the top of the stirred vessel.

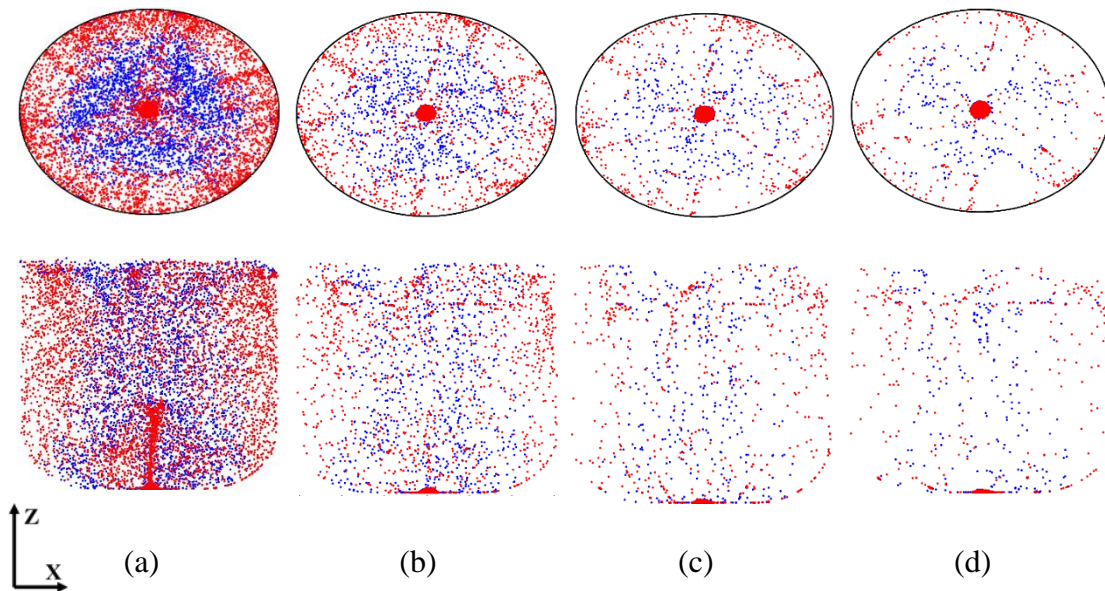


Figure 4.3 Poincaré maps of solids of different crystal density (a)1300kg/m³, (b) 1770 kg/m³, (c) 2340 kg/m³ and (d) 2750 kg/m³ for the top view (top row) and front view (bottom row)

It is observed in Figure 4.3(a) that the particles are flowing along the axis of the impeller. The particles in the draft tube region are flowing downwards and the particles in the annulus region is flowing upwards forming a continuous circulatory motion (chaotic motion). As the density of the particle increases to 1770 kg/m³ the particles are uniformly circulating in the stirred vessel but the suspension density of the particle has reduced in Figure 4.3(b). Therefore, as the particle density increases to 2340 kg/m³, and higher i.e., 2750 kg/m³, the distribution of the particle become non uniform and more chaotic as found in Figure 4.3(c) and (d).

Table 4.3 Shannon's entropy and the uniformity in the stirred vessel

Sl. No	Particle density, kg/m ³	Shannon's entropy	Uniformity
1	1300	6.9371	0.7201
2	1770	6.8052	0.6311
3	2340	6.6018	0.515
4	2750	6.3917	0.4174

It is found in Table 4.3 that the Shannon's entropy reduces with the increase in the particle density. Hence it is recommended to use DTB-IV configuration for densities lower than 2750 kg/m³ as the crystals may not distribute uniformly in the stirred vessel.

In order to investigate the suspension quality of solids volume fraction greater than 10%, Lagrangian approach is not valid. Hence to analyse the suspension characteristics for dense solid loading, CFD simulations are performed using the Euler-Granular model. Particles of 0.5 mm diameter and specific gravity (SG = 2.34) is introduced in the stirred vessel to predict the suspension density and cloud height. The predicted iso-contours of solid volume fraction for various draft tube configurations are shown in Figure 4.4. Here red colour indicates higher volume fraction of solids (0.65) and the blue indicates zero volume fraction. It is found that sedimentation of particles occurs at the vessel bottom in the absence of outer baffles, and complete suspensions of solid particles are observed when DTB-IV and DTB-V are used. Thus, the baffle supports overcoming the sedimentation of solids in a liquid-solid system.

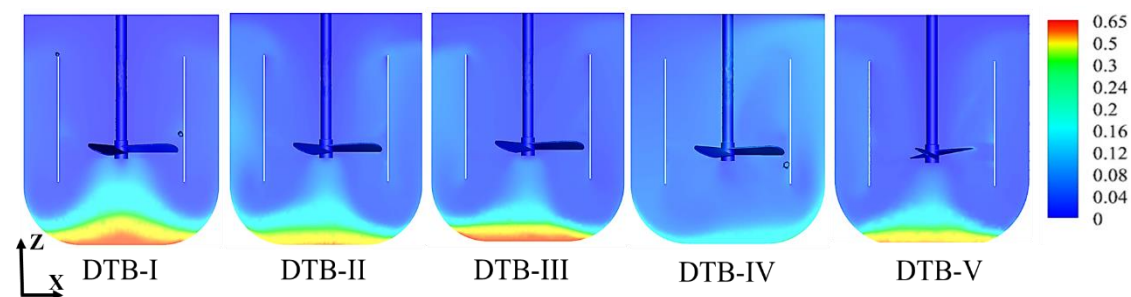


Figure 4.4 Iso-contours of the volume fraction of solids (Y= 0.005m).

To quantify this further, the mass-weighted uniformity index is calculated (Wu

2014). This indicates the uniformity of the solid concentration across the surface. Its magnitude varies from 0 (incomplete suspension) to 1 (homogenised suspension). To evaluate this, a vertical plane is chosen at $Y = 0.008$ m, and the average mass-weighted uniformity (γ_m) is calculated for the entire liquid volume in the stirred vessel.

$$\gamma_m = 1 - \frac{\sum_1^n [(\phi_i - \phi_m)](|\rho_i \bar{v}_i A_i|)}{2|\phi_m| \sum_1^n (|\rho_i \bar{v}_i A_i|)} \quad (4.37)$$

Table 4.4 Mass uniformity index and cloud height for various draft tube configuration

Sl. No	Name	Mass avg. uniformity index (γ_m)	Cloud height (H _c /H)
1	DTB-I	0.4	0.82
2	DTB-II	0.5	0.88
3	DTB-III	0.5	0.89
4	DTB-IV	0.9	0.97
5	DTB-V	0.8	0.96

This is reported in Table 4.4 for various draft tube configurations. The value of the mass-weighted uniformity index is observed to be very low for draft tube systems DTB-I to DTB-III (0.4 to 0.5). This indicates only 40- 50% of the solids are uniformly distributed. However, its value is found to be larger when for DTB-IV and DTB-V. This indicates 80 – 90% of suspension of solids in the stirred vessel. This is further verified by analysing the cloud height in the stirred vessel system. This describes the height at which the solids are lifted up till clear distinction between solid and liquid phases are observed (Ochieng and Onyango 2010). This is calculated by plotting the solid concentration along with the height of the stirred vessel. The height at which the solid concentration becomes zero is treated as cloud height (Ochieng and Lewis 2006). The calculated values are reported in Table 4.4, and the magnitude of cloud height is found to be high when DTB-IV is used. Since the DTB-IV configuration creates secondary recirculation at the bottom of the vessel, it supports the complete suspension of solid particles. Thus, DTB –IV configuration with three internal baffles and six

external baffles (90° angle) is more advantageous in improving liquid circulation, mixing and overcoming sedimentation of solids in a stirred vessel.

4.4 Summary

To find the performance of solid suspension in stirred vessels, particle is introduced at the top of the vessel in a Lagrangian way. The performance of solids suspension in an unbaffled stirred vessel is improved by introducing a draft tube baffle. The predicted trajectories of the particles are analysed qualitatively using Poincaré maps and was quantified through Shannon entropy. The Shannon entropy magnitude is found to be maximum in the baffled stirred vessel (DTB-IV). Further, the effect of the particle density on the suspension quality is analysed. It was found that as the particle density increases the quality of the particle suspension lowers. Hence it supports proper mixing of particles whose density is lesser than 2750 kg/m^3

To investigate the sedimentation of dense solid concentration, $500 \mu\text{m}$ size particles are introduced at the vessel bottom. This is modelled through the Euler-Granular approach to quantify the solid concentration through normalised cloud height, and mass averaged uniformity index. This is analysed for various baffle configurations, and it was found that DTB-IV has the highest uniformity of solid particles.

CHAPTER 5

CRYSTALLIZATION IN STIRRED VESSELS

5.1 Introduction

A batch stirred vessel system has a major application in crystallization. The crystallizer is used to obtain pure crystalline materials with a controlled size range and shape (Sulttan and Rohani 2019). These characteristics of the crystal control the downstream processing steps such as filtration and drying (Szilágyi and Nagy 2018). The quality of crystals strongly depends on various operating conditions in a crystallizer such as local supersaturation, hydrodynamics, fluid mixing, and geometry, modes of crystallizer operation, seeding, aggregation, breakage and hence the crystal size distribution (CSD) (Rohani et al. 2005a; de Souza et al. 2021).

Since the dependence of growth and nucleation rates on supersaturation is highly system-specific, the determination of the optimum conditions that produce the desired crystalline product requires numerous bench-scale experiments. These conditions might not be optimal after the crystallizer's scaling-up, as the mixing affects supersaturation (Green 2002; Paul et al. 2004). This motivates us to use the computational fluid dynamics CFD model to predict the crystallization process and quantify the effects of flow-induced mixing on crystal size distribution (CSD).

5.2 Methodology

5.2.1 Physical properties of KH_2PO_4

The physical properties of the solution (continuous phase) and the crystals are mentioned in Table 5.1. Since the temperature range of operation is 298 to 323 K, the solution density and viscosity does not change significantly, and the average values are used. The physical properties are considered to be constant in CFD calculations.

Table 5.1 Physical properties of the solution and the crystals

Sl. No	Property	Value	Units
1	Density (solution) (ρ)	1170	kg/m ³
2	Dynamic viscosity (solution) (μ)	0.0015	Pa. s
3	Diffusion coeff. (D)	5.7 x 10 ⁻¹⁰	m ² /s
4	Density (crystal) (ρ_c)	2340	kg/m ³
5	Volumetric shape factor (k_v)	0.75	-
6	Molar mass (M)	136	g/mol
7	Specific heat (Cp)	857	J/(kg. K)
8	Thermal conductivity (k)	1.34	W/(m. K)
9	Heat of crystallization	-1.569 x 10 ⁹	J/kmol

5.2.2 CFD modelling

The crystal size distribution in the stirred vessel is predicted using population balance equations (PBE). The PBE is described using the number density function (NDF), and it is given (particle volume, V) by

$$\begin{aligned}
 \frac{\partial}{\partial t} [n(V, t)] + \nabla \cdot [\vec{u}n(V, t)] + \underbrace{\nabla_V \cdot [G_V n(V, t)]}_{\text{Growth term}} = \\
 \underbrace{\frac{1}{2} \int_0^V a(V - V', V') n(V - V', t) n(V', t) dV'}_{\text{Birth due to Aggregation}} - \underbrace{\int_0^\infty a(V, V') n(V, t) n(V', t) dV'}_{\text{Death due to Aggregation}} + \\
 \underbrace{\int_{\Omega_v} p g [V'] \beta (V|V') n(V') dV'}_{\text{Birth due to Breakage}} - \underbrace{g(V) n(V, t)}_{\text{Death due to breakage}} \quad (5.1)
 \end{aligned}$$

Here n represents the number density of particles of volume V at time t . The initial and boundary conditions are

$$n(V, t = 0) = n_v; \quad n(V = 0, t) G_v = B \quad (5.2)$$

where, $n(V, t)$ is number density function, G_v is the growth rate based on the volume of the particle, n_v is the initial number density of the seed crystals, B is the nucleation rate ($\# / \text{m}^3 \cdot \text{s}$). Since the magnitude of agglomeration is insignificant for crystal size greater than $50 \mu\text{m}$ (Mersmann 2001), crystal breakup and agglomeration are not considered in the present work. Thus, Eqn (5.1) becomes,

$$\frac{\partial}{\partial t} [n(V, t)] + \nabla \cdot [\vec{u}n(V, t)] + \underbrace{\nabla_V \cdot [G_v n(V, t)]}_{\text{Growth term}} = 0 \quad (5.3)$$

The single particle volume (V) is given by

$$V = k_v L^3 \quad (5.4)$$

The relationship between G_v (volume growth) and G (linear growth) is

$$G_v = 3 k_v L^2 G \quad (5.5)$$

The volumetric shape factor (k_v) for KH_2PO_4 crystal is 0.75. The growth (G) and nucleation (B) kinetics for KH_2PO_4 – water system is implemented using a user-defined function (UDF) in CFD commercial software package (ANSYS Fluent v 2020R3). The solubility data, nucleation and growth kinetics for KH_2PO_4 crystals are taken from the experimental investigations of KDP (Temmel et al. 2016a)

$$B = 5.2 \times 10^{-2} e^{\left(\frac{-10000}{RT}\right)} (S - 1)^{5.8} \quad (5.6)$$

$$G = 5.1 \times 10^6 e^{\left(\frac{-70000}{RT}\right)} (S - 1)^{1.26} \quad (5.7)$$

$$S = c(t) / c^*(\theta) \quad (5.8)$$

$$c^*(\theta) = 15.24 + 0.206 \theta + 1.01 \times 10^{-2} \theta^2 - 1.45 \times 10^{-4} \theta^3 + 1.23 \times 10^{-6} \theta^4 \quad (5.9)$$

where B ($\#/\text{m}^3 \cdot \text{s}$) is the nucleation rate, R (J/mol. K) is the universal gas constant, T (K) is the solution mixture temperature, G (m/s) is the growth rate of the crystals, S is the relative supersaturation, $c^*(\theta)$ saturation concentration of KH_2PO_4 at the temperature ($^\circ\text{C}$) and $c(t)$ is the concentration of the KH_2PO_4 solute at time instant (s). The crystallization kinetics [(5.6) and (5.7)] are valid when the solution is supersaturated (i.e., $S > 1$).

The PBEs are solved using the quadrature method of moments (QMOM) (McGraw 1997). The QMOM approach is computationally inexpensive with relatively high accuracy when compared to other methods (Marchisio et al. 2003). The quadrature

approximation is based on determining a sequence of polynomials orthogonal to the particle size distribution $n(L)$.

$$\mu_k = \int_0^\infty f(L)n(L)dL = \int_0^\infty n(V,t) L^k dL \approx \sum_{i=1}^N f(L_i)\omega_i \quad (5.10)$$

where ω_i is the weights and L_i is the abscissas that are determined using the product difference (PD) algorithm from the lower order moments. The “N” is the order of approximation, and k is the specified number of moments used to solve the PBE. The Eqn (5.3) is transformed using Eqn (5.10). The initial moment's distribution is obtained using (Hemalatha and Rani 2017).

$$\mu_i^s = N_s L_s^i \quad (5.11)$$

where, μ_i^s is the i^{th} moment with $i = 0, 1, 2, \dots, 5$; L_s is the size of the seeded crystals, N_s is the number of seed crystals, and it is calculated by

$$N_s = \frac{M_s}{\rho_c k_v L_s^3} \quad (5.12)$$

where M_s is the mass of the seed crystals introduced in our stirred vessel, k_v is the volume shape factor, ρ_c is the density of KH_2PO_4 (2340 kg/m^3). The moments obtained at the end of the flow simulation time is reconstructed to obtain crystal size distribution (CSD) (John et al. 2007). The PBE is coupled with Euler - Granular model through the Sauter mean diameter ($d_{32} = \mu_3 / \mu_2$) to calculate the interfacial properties, namely drag force. The third-order moment (μ_3) is related to the volume fraction of the dispersed (particle) phase is,

$$\alpha_s = k_v \sum_{q=1}^N \omega_q L_q^3 \quad (5.13)$$

The sum of volume fraction of continuous (liquid) and dispersed (particle) phase are considered to be unity, i.e.,

$$\sum_{q=1}^{n_p} \alpha_q = 1 \quad (5.14)$$

The conservation equation for continuity and momentum are

$$\underbrace{\frac{\partial}{\partial t} (\alpha_q \rho_q)}_{\text{Transient}} + \underbrace{\nabla \cdot (\alpha_q \rho_q \vec{v}_q)}_{\text{Convective}} = \underbrace{\sum_{p=1}^{n_p} m_{pq}}_{\text{interphase mass exchange}} \quad (5.15)$$

where α , ρ , \vec{v}_q are the volume fraction, density and velocity of the q phase respectively.

$$\begin{aligned}
\underbrace{\frac{\partial}{\partial t}(\alpha_q \rho_q \vec{v}_q)}_{\text{Transient}} + \underbrace{\nabla \cdot (\alpha_q \rho_q \vec{v}_q \vec{v}_q)}_{\text{Convective}} = \underbrace{-\alpha_q \nabla p}_{\text{Pressure}} - \underbrace{\nabla \cdot \bar{\bar{\tau}}_q}_{\text{shear}} + \underbrace{\alpha_q \rho_q \mathbf{g}}_{\text{body}} + \\
\Sigma \left(\underbrace{R_{pq}}_{\substack{\text{interphase force} \\ \text{exchange}}} + \underbrace{m_{pq} \vec{v}_q}_{\substack{\text{interphase force} \\ \text{exchange}}} \right) + \underbrace{\alpha_q \rho_q F_{td,q}}_{\text{Drag force}} \quad (5.16)
\end{aligned}$$

where P is particles pressure, R_{pq} is the interaction force, \vec{v}_q is the interphase velocity. The 2nd term on the RHS of Eq. (5.16) represents momentum flux $\bar{\bar{\tau}}$ due to particle stress-strain tensor, 3rd term is the body force term, 4th term accounts for interaction force between the two phases.

The interphase force exchange term is modelled using phase velocities,

$$R_{pq} = K_{ls}(\vec{V}_l - \vec{V}_s) \quad (5.17)$$

where, K_{ls} is the interphase momentum exchange coefficient, and it depends on drag function and particle relaxation time. The drag model given by Gidaspow (Ding and Gidaspow 1990) is used to predict the interphase momentum exchange (K_{ls}).

The dispersed k- ϵ turbulence model used to predict liquid phase turbulence

$$\frac{\partial}{\partial t}(\alpha_l k_l) + \nabla \cdot (\vec{V}_l \alpha_l k_l) = \nabla \cdot \left(\alpha_l \left(\mu_l + \frac{\mu_{t,l}}{\sigma_k} \right) \nabla k_l \right) + \alpha_l G_{k,l} + -\alpha_l \epsilon + \alpha_l \pi_{kl} \quad (5.18)$$

$$\frac{\partial}{\partial t}(\alpha_l \epsilon_l) + \nabla \cdot (\vec{V}_l \alpha_l \epsilon_l) = \nabla \cdot \left(\alpha_l \left(\mu_l + \frac{\mu_{t,l}}{\sigma_\epsilon} \right) \nabla \epsilon_l \right) + \alpha_l \frac{\epsilon_l}{k_l} (C_{1\epsilon} G_{k,l} - C_{2\epsilon} \epsilon_l) + \alpha_l \pi_{\epsilon l} \quad (5.19)$$

where $G_{k,l}$ is the turbulence kinetic energy production due to mean velocity.

5.2.3 Simulation Methodology

To predict the crystal size distribution, the KH_2PO_4 - water system is considered. CFD simulations are performed using QMOM to discretize the PBE. To account for the equilibrium solubility, temperature and solute concentration, the growth and nucleation rate is defined through a user-defined function (UDF). The UDF uses the physical

properties of dissolved KH_2PO_4 in H_2O . The UDF first calculates the equilibrium solubility using equation (5.9). This depends on the solution temperature (θ). The calculated solubility of KH_2PO_4 in water is used in equation (5.8), and supersaturation is computed by considering the mass fraction of KH_2PO_4 . The nucleation and growth rate are predicted through equation (5.6) and (5.7), respectively incorporating solution temperature (T) and supersaturation data at every computational cell. The constituent KH_2PO_4 in water is modelled as a species in the primary phase. The CFD simulation is initialized with a KH_2PO_4 mass fraction of 0.32, solution temperature of 308 K and relative supersaturation at 1.05. The walls of the stirred vessel are maintained at 298 K. Here transient CFD simulations are performed with an adaptive time step (Δt) of 10 μs . The convergence criterion for all residuals is set to be 10^{-6} .

5.3 Results and discussion

The performance of the crystallization process is investigated by introducing the baffle configuration for a stirred vessel. The nucleation and growth in the crystallisation process in the stirred vessel are investigated. The initial temperature of the supersaturated solution is considered to be 308 K, and the walls of the stirred vessel are cooled to 298 K. As the temperature of water decreases due to cooling, the solubility of KH_2PO_4 decreases and hence its supersaturation increases. The local supersaturation is calculated using a UDF. As supersaturation influences the nucleation and crystal growth rate in the stirred vessel system, it is analysed for unbaffled and baffled stirred vessel.

The predicted contours of local supersaturation ($y = -0.005 \text{ m}$) are shown in Figure 5.1. It is observed that the magnitude of supersaturation is found to be uniform in the baffled and non-uniform in the unbaffled stirred vessel system. This is attributed to the significant extent of mixing among the fluid elements in the baffled stirred vessel. Since the magnitude of temperature distribution is found to be low at the bottom of the unbaffled stirred vessel. The supersaturation value is found to be high at the bottom of the unbaffled stirred vessel. These predictions once again support baffled stirred vessel configuration.

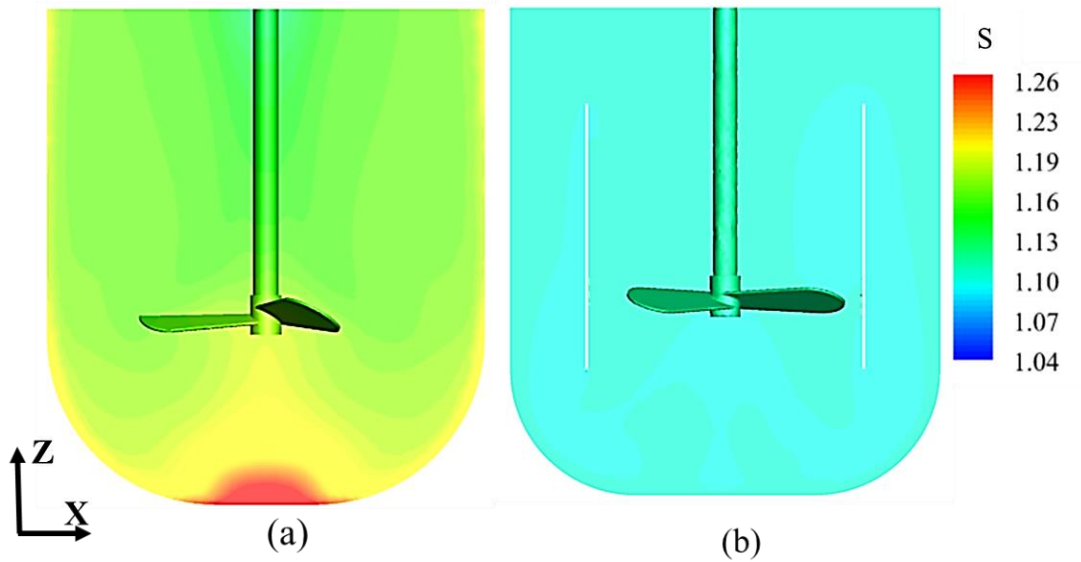


Figure 5.1 Contours of supersaturation (a) un baffled and (b) baffled stirred vessel

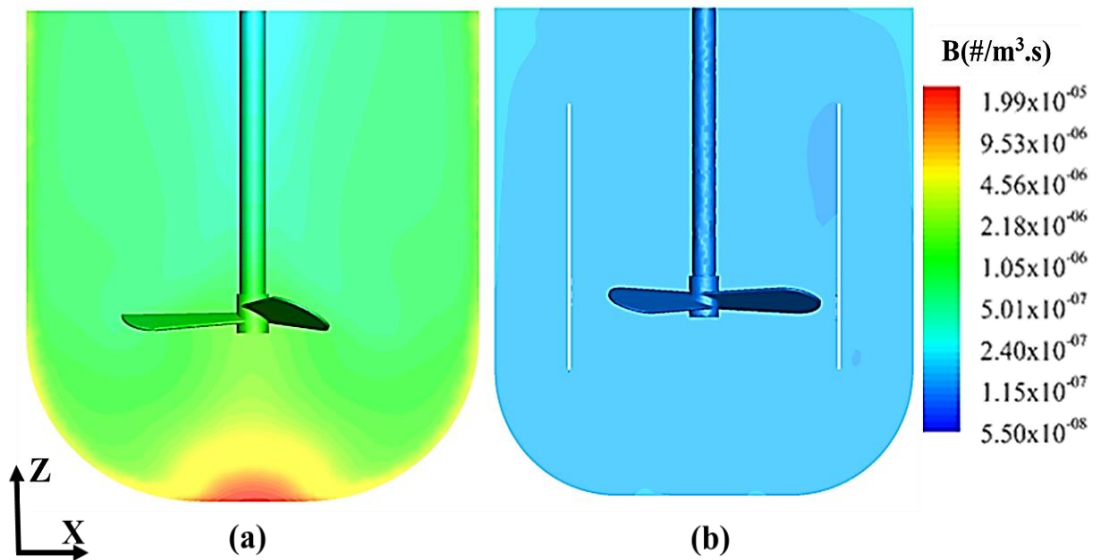


Figure 5.2 Contours of nucleation rate (a) un baffled and (b) baffled stirred vessel

Further, the predicted nucleation rate is analysed along $y = -0.005$ m. This is shown in Figure 5.2. It is observed that the variation of the nucleation rate is found to be insignificant in the baffled stirred vessel system and significant for the un baffled system. This is attributed to strong re-circulatory flow in the baffled stirred vessel. Since nucleation depends on supersaturation, contour plots (Figure 5.1, 5.2) looks similar.

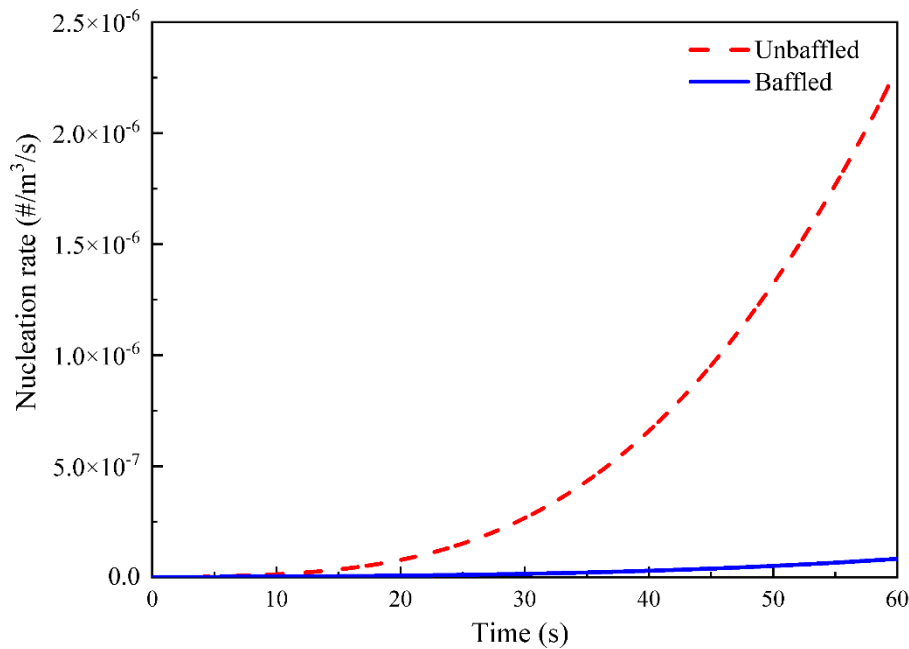


Figure 5.3 Temporal variation nucleation rate for the stirred vessel system

The nucleation rate is quantified and shown in Figure 5.3 for the baffled and unbaffled stirred vessel. The volume-weighted average rate of nucleation increases exponentially with time in the unbaffled system due to the formation of small nuclei on the surface of the seed crystal. Hence, seed crystals growth rate would be at a slower rate. Thus, the expected yield of the crystals would be less in the unbaffled stirred vessel.

To quantify the crystallization process of KDP crystals, the predicted zeroth moment (total number of crystals per unit volume of mixture suspension) is analysed for the baffled and unbaffled system. This is shown in Figure 5.4. The increase in the zeroth moment indicates the formation of new small crystals from the solution. The formation of the new small crystals depletes the concentration of the solute. This characterizes the resistance due to the mass transfer of the solute to the number of seed crystals. In the baffled system, the zeroth moment value is observed to be constant. This indicates that the extent of nucleation is insignificant than the growth of the crystals. However, in the unbaffled system, the magnitude of the zeroth moment is observed to be higher. This leads to a significant extent of nucleation and hence non-uniform product size in the unbaffled system.

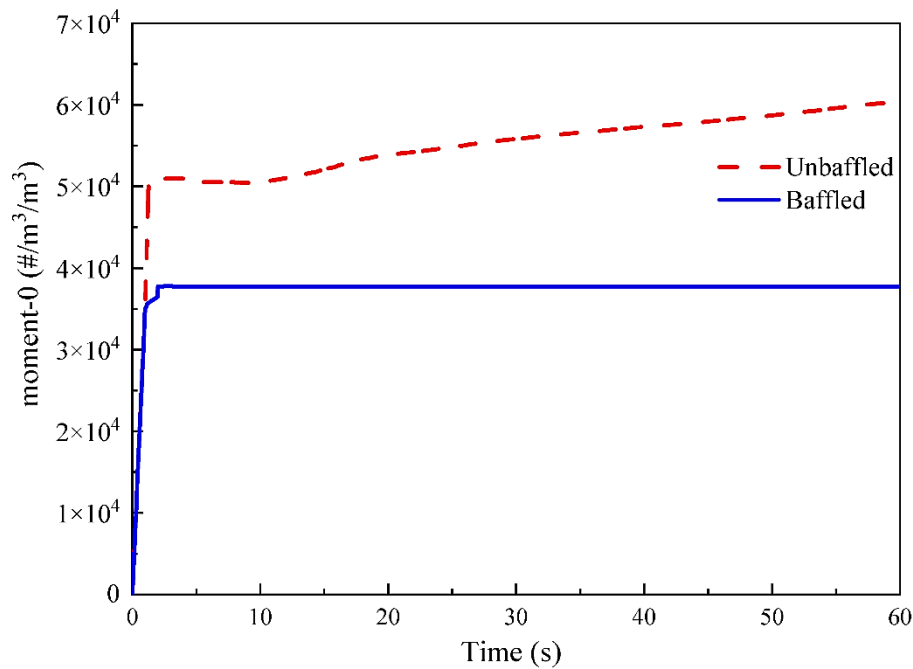


Figure 5.4 Temporal variation of the zeroth moment (m_0) of the stirred vessel systems

This is attributed to the formation of new crystals due to the higher nucleation rate. Thus, it affects the flowability of crystals in the unbaffled system. Thus, longer batch times are required to obtain a higher yield in an unbaffled stirred vessel system. Here, the baffled system is found to be more advantageous to carry out the crystallization process.

The crystal size distribution (CSD) is reconstructed from the finite set of moments (John et al. 2007) obtained by solving full PBEs. The first six moments are used to reconstruct the CSD using the spline-based method (John et al., 2007). Here the piecewise polynomial function is used to approximate the shape of the distribution. The CSD is reconstructed using cubic spline in an iterative manner using MATLAB.

The CSD determines the quality of the crystallization process. Here, seed particles of size 500 μm are introduced, and their effects on the CSD are analyzed for unbaffled and baffled stirred vessel configuration. This is shown in Figure 5.5. A significant difference in CSD is observed for unbaffled and baffled stirred vessel systems. The CSD is found to be narrow for the baffled system (area, 37752) and broader for the unbaffled system (area, 65214). The broader distribution in the unbaffled stirred vessel is attributed to the spatial inhomogeneity of supersaturation.

The area under the curve indicates the number of crystals that are formed during the crystallization process. The number of crystals in the baffled system is found to be 42% lower than the un baffled system. This indicates a more significant number of nucleated crystals in the un baffled stirred vessel system, which is undesirable.

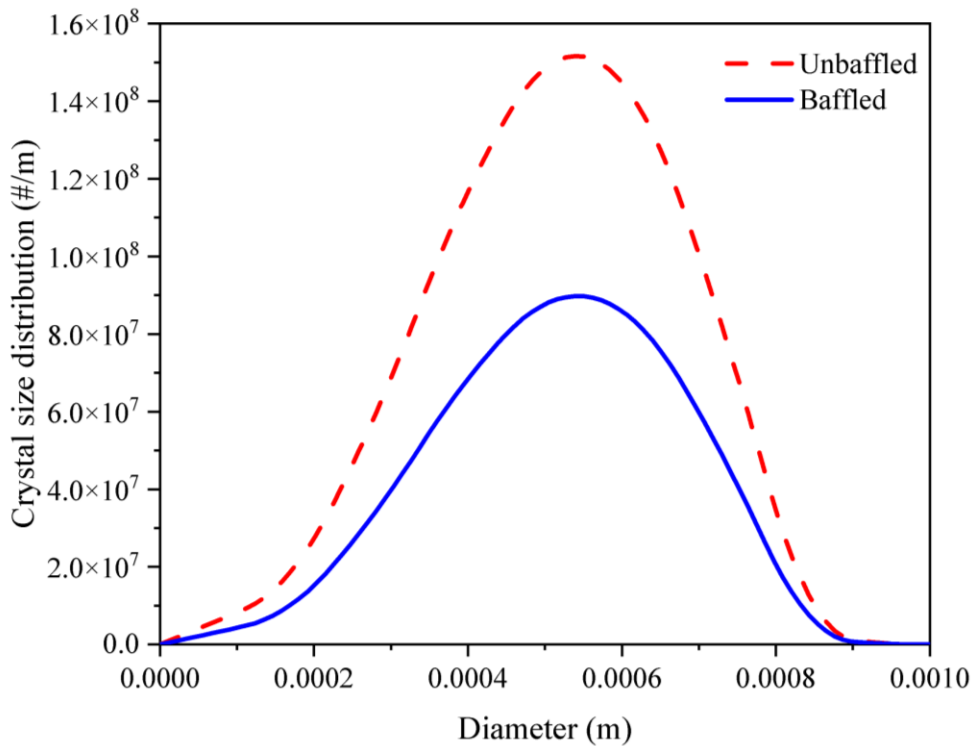


Figure 5.5 The crystal size distribution of the stirred vessel systems

This is further quantified by calculating statistical parameters such as De Brouckere mean diameter (d_{43} , moment-4 /moment-3), coefficient of variation (COV), and number mean diameter (d_{10} , moment-1/moment-0) and are reported in Table-5.2. It is observed that the magnitude of number mean diameter (d_{10}) and De Brouckere mean diameter (d_{43}) are higher for the baffled stirred vessel, indicating a higher growth rate.

Table 5.2 Statistical reports of the un baffled and baffled stirred vessel system

Stirred vessel type	Un baffled	Baffled
De Brouckere mean diameter (d_{43}) (μm)	514	520
Number mean diameter (d_{10}) (μm)	513	516

Stirred vessel type	Unbaffled	Baffled
B/G	4.61	0.25

Since growth and nucleation rate are dependent on the supersaturation concentration, the ratio of nucleation (B) to the growth rate (G) is calculated. This is shown in Table 5.2. The value of B/G is found to be low for the baffled and high for the unbaffled stirred vessel systems. This is attributed to the significant growth of KH_2PO_4 crystals and insignificant nucleation in the baffled stirred vessel system. Thus, the baffled stirred vessel system is more advantageous to carry out the crystallization process, and hence further investigations are focused on the baffled stirred vessel.

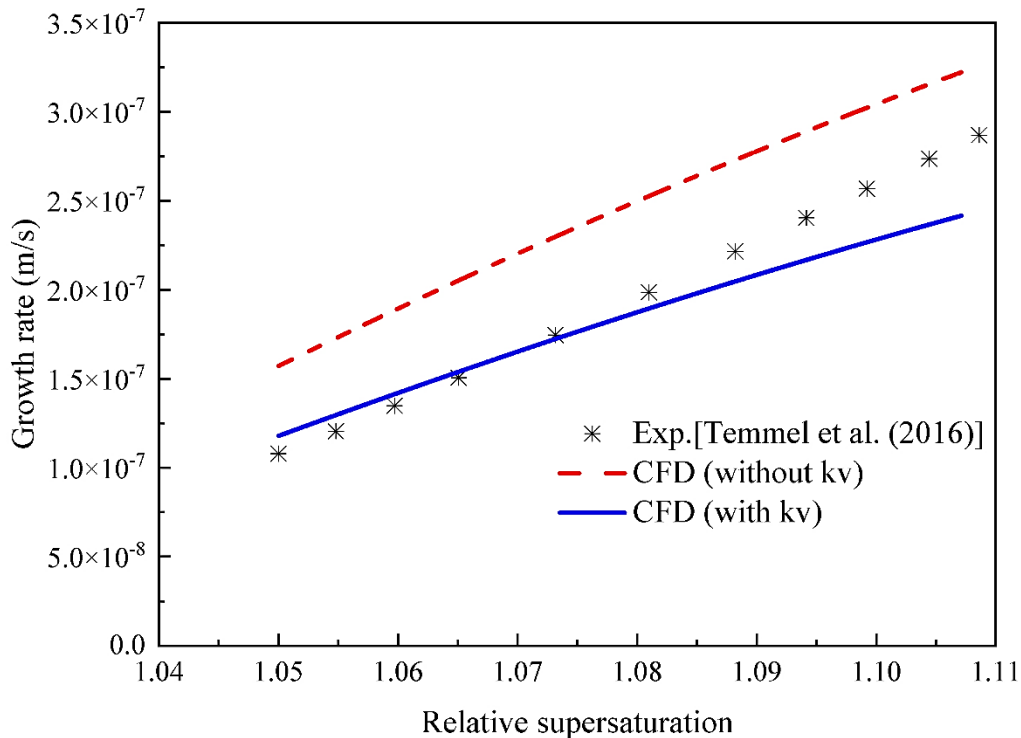


Figure 5.6 Comparison of experimental data of growth rate and supersaturation with CFD simulations including and excluding shape factor (k_v) in the baffled stirred vessel

The growth rate of KH_2PO_4 (KDP) crystals is calculated using equation (5.8) for various supersaturations. This is compared with experimental data of Tommel et al. (2016) and is shown in Figure 5.6. It is observed that the growth rate of KH_2PO_4 crystals increases linearly with supersaturation. The calculated error between numerical and experimental data is found to be 25%, and it decreased to 7.5% by incorporating volume

shape factor ($k_v = 0.75$) in the growth kinetics (equation 5.8). Hence, the volume shape factor of crystals is found to be an essential parameter for accurate prediction of crystal growth in the batch stirred vessel system (Mersmann 2001).

To ensure narrow crystal size distribution with excellent flowability and to minimize the nucleation rate, seed crystals (KH_2PO_4) are introduced into the baffled stirred vessel system. However, limited information is available in the literature on the amount and size of seed crystals to be added, giving the desired CSD. Hence, different amount of seed crystals such as 100 g, 500 g, 750 g and 1000g with 500 μm size diameter are needed to find an optimum seeding condition that can improve a poorly behaved crystallization process. The predicted crystal size distribution (CSD) for various amounts of seed crystals are shown in Figure 5.7. The narrow size distribution is observed when 750 g of seed crystals are used. These predictions are quantified further by calculating the De Brouckere mean diameter (d_{43}) and mass of the seed crystals that are crystallized, and it is depicted in Table 5.4. The De Brouckere mean diameter (d_{43}) is observed to be high when 750 g of seed crystals are used. The crystallized mass increases with the number of seed crystals. It is uneconomical to use more than 5% of solids concentration (Mersmann 2001) for the seeded crystallization process. Hence 750 g is considered to be a desirable amount of seed crystals that gives narrow distribution.

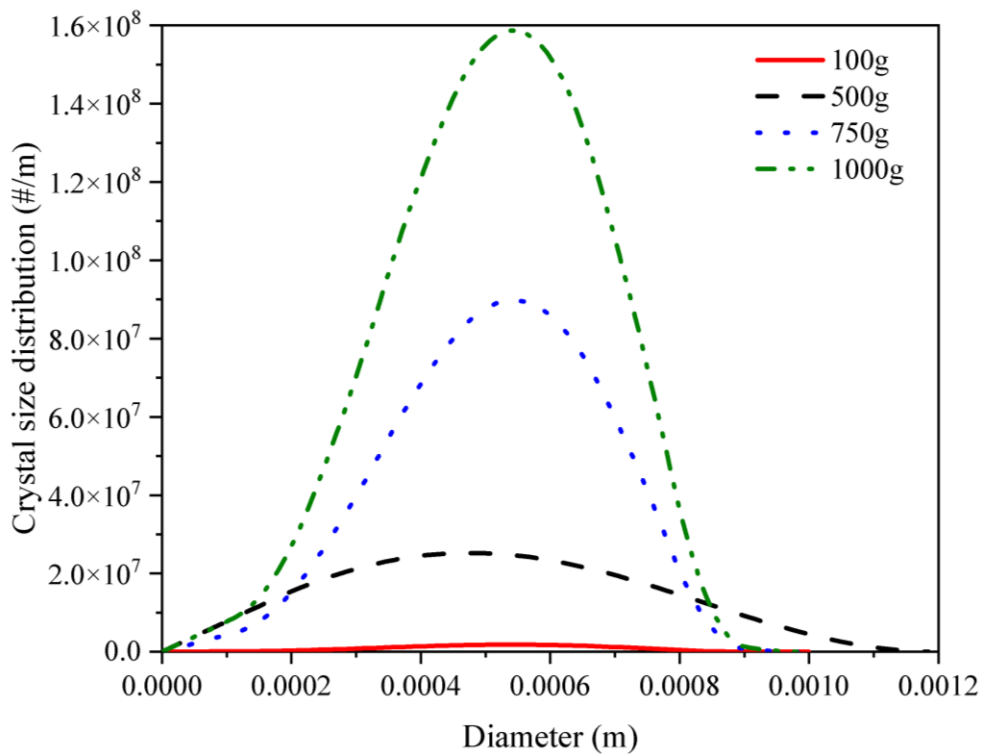


Figure 5.7 Effect of different seed mass on CSD

Table 5.3 Effect of seed crystal amount on the mean size and crystallized mass

Seed mass (g)	100	500	750	1000
De Brouckere mean diameter (d_{43}) (μm)	508	514	520	515
Crystallized mass (g)	0.0004	0.012	2.72	4.8

To predict crystal size distribution in the stirred vessel system, KH_2PO_4 seed crystals of different size range (100 – 700 μm) are introduced in the batch stirred vessel. The crystal size distribution is reconstructed from the moments, and it is shown in Figure 5.8. The crystal size distribution is found to be broader when the seed crystal size is larger than 500 μm , and it is narrow when the seed crystal size is less than 500 μm . As the batch time for crystal growth is longer for the seed crystal size greater than 500 μm , broader crystal size distribution is observed. Once again, statistical parameters such as De Brouckere mean diameter (d_{43}), COV, and mass of the seed crystals that are crystallized, are calculated to quantify the crystal size distribution. This is reported in Table 5.4.

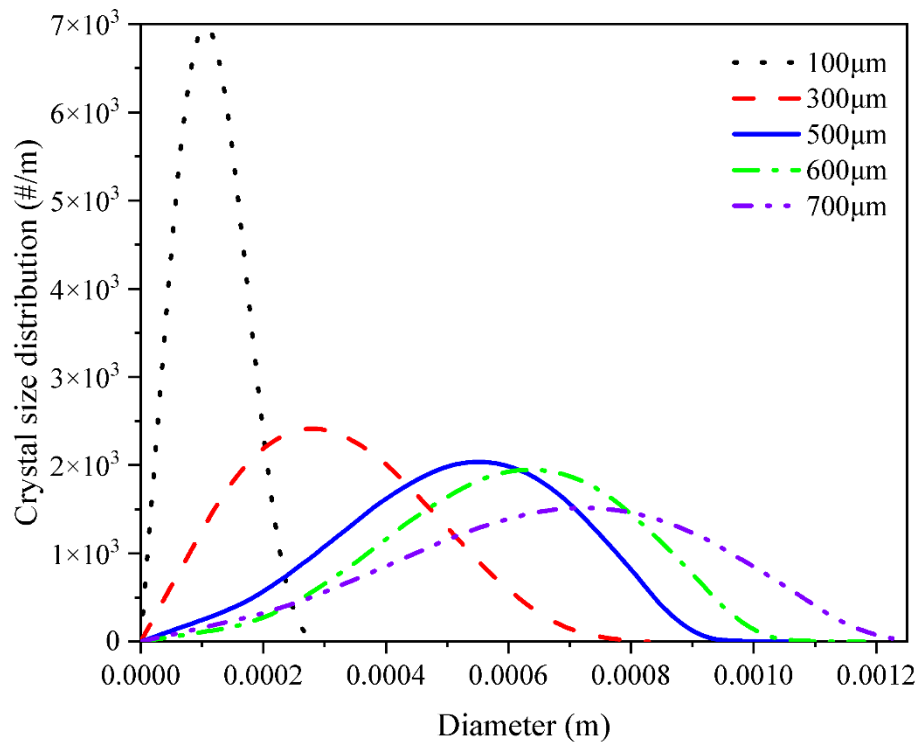


Figure 5.8 Effect of seed crystal size on the CSD.

It is observed that the De Brouckere mean diameter (d_{43}) is smaller when seed crystals size is greater than 500 μm . This size (500 μm) is considered the critical size and above which primary nucleation occurs on the seed surface. Due to surface nucleation, the De Brouckere mean diameter is found to be smaller for seed size greater than 500 μm . Figure 5.8 is a qualitative comparison, and it is quantified through the coefficient of variation (COV) shown in table 5.4. The smaller the value of COV indicates a narrow CSD. The magnitude of COV for 500 μm is 0.56, and for 100 μm is 0.93. The calculated coefficient of variation (COV) is observed to be minimum for 500 μm seed crystal size. Hence 500 μm (seed size) is considered to be optimum. The calculated mass of seed crystallized shows that its magnitude is considerably larger for seed crystal size greater than 500 μm . This is attributed to surface nucleation rather than growth. Hence, the smaller seed crystal size ($< 500 \mu\text{m}$) supports narrow crystal size distribution by suppressing primary nucleation.

Table 5.4 Effect of seed crystal size on mean diameter, COV and crystallized mass

Seeding size (μm)	100	300	500	600	700
De Brouckere mean diameter (d_{43}) (μm)	140	330	520	550	660
COV	0.93	0.78	0.56	0.78	0.8
Crystallized mass (g)	0.13	0.73	2.72	5.19	10.63

The effect of seeding temperature on crystal growth (KH_2PO_4) is numerically analyzed for 303 K, 308 K, 318 K and 323 K in the baffled stirred vessel. The solution temperature is maintained the same as the seed crystal temperature. The seed crystals are injected into the region between the metastable zone width and solubility curve (Temmel et al. 2016a). For various seeding temperature, solubility data are calculated using Temmel et al. (2016). The solubility is maintained at 1.05 so that the extent of nucleation is insignificant. Here, the stirred vessel walls are maintained at 298 K. The growth and nucleation rates are shown in Figure 5.9 (a-b).

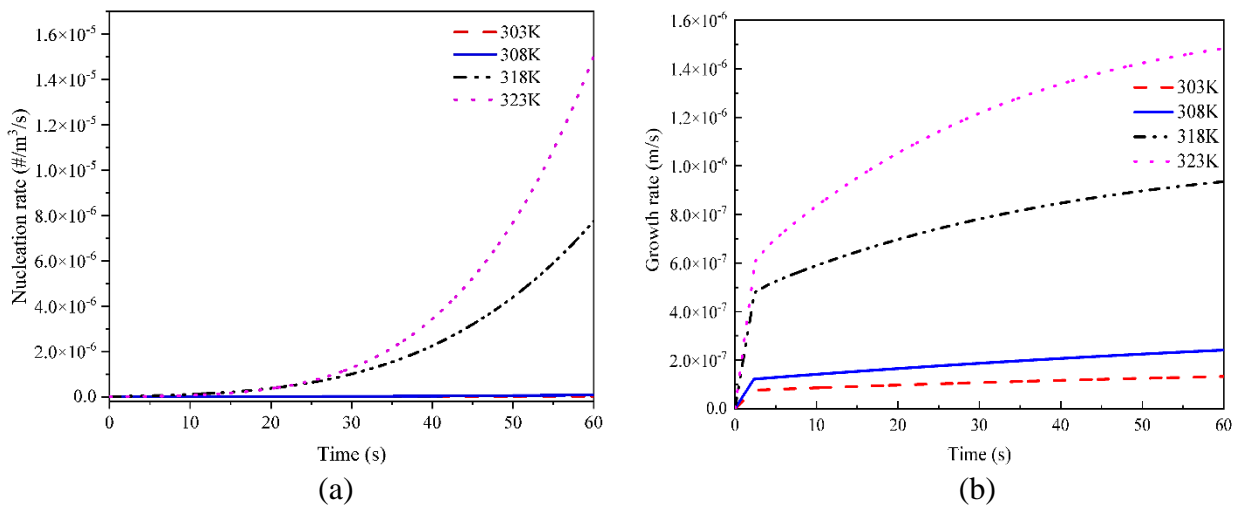


Figure 5.9 Evolution of (a) nucleation and (b) growth rates for various seed crystal temperatures

It is found that the growth (equation 5.8) and nucleation rate (equation 5.7) is increasing linearly with an increase in the seeding temperature. Since the difference between seed crystal and wall temperature is related to the supersaturation, at higher seed crystal temperature (323 K), growth and nucleation rate are observed to be maximum. Also, at

the higher temperature (323 K), both crystal growth (KH_2PO_4) and surface nucleation occur. In order to find a suitable temperature that supports the crystallization process, the ratio of nucleation overgrowth is calculated. This is reported in Table 5.6. It is observed that its value is significantly larger when seed crystals temperature is greater than 308 K. When the ratio of B/G is greater than 1 (i.e., $T > 308$ K), uncontrolled nucleation occurs in the stirred vessel system, which is undesirable but when B/G is less than 1 (i.e., $T < 308$ K) only crystal growth occurs (controlled nucleation).

Table 5.5 Effect of seeding temperature on nucleation (B)/ growth (G)

Seeding Temperature (K)	303	308	318	323
B/G	0.2	0.3	8.3	10.1

Hence, 308 K is considered as the optimum seeding temperature that supports crystal growth over nucleation. Hence it is advantageous to maintain a temperature difference of less than 10 K.

5.4 Summary

The applicability of the stirred vessel system for crystallization of KDP - water system is investigated. The nucleation, growth and crystal size distribution (CSD) is predicted using the population balance model (PBM). The performance of the baffled stirred vessel is found to be superior over the unbaffled system. The crystal size distribution is found to be broader in the unbaffled system due to the higher nucleation rate. The importance of volume shape factor (k_v) on crystal growth is analysed and found to be necessary for accurate prediction of crystal growth. Further, the effect of seed crystal amount and size on CSD is studied. The crystal size distribution is found to be narrow when seed crystals of 750 g mass and 500 μm size are used. Hence, this seed mass and size is considered to be optimum. The effect of seeding temperature on nucleation and growth rate is analysed. The performance of crystallisation is found to be better at lower seed crystal temperature (308K). Thus, nucleation, crystal growth and crystal size distribution of KH_2PO_4 are strongly dependent on local supersaturation, type of stirred vessel and seed amount and temperature distribution in a stirred vessel system.

Thus, this combined (CFD-PBM) approach helps understand the crystallization process in a batch stirred vessel system. The predicted results from this study could be important to assure efficient industrial operations of the batch crystallizer.

CHAPTER 6

CONCLUSIONS

The flow field in the unbaffled and baffled stirred vessel is numerically analyzed using CFD. It was found that baffled system supports enhancing the liquid circulation in the region below the impeller, and 300 rpm was found to be optimum impeller speed.

To improve the liquid circulation and mixing, various geometric modifications were made in the stirred vessel. It is found that the DTB-IV configuration is more advantageous in enhancing the flow field. The suspension quality is investigated for various geometry modifications. The suspension quality was simulated using Lagrangian approach for low solid concentration and Euler-Granular approach for high solid concentration. The suspension quality was analyzed through Poincaré maps and the concept of Shannon entropy. It was found that DTB-IV performs better at dilute concentrations. Further for dense concentration the suspension quality was quantified through cloud height and uniformity. DTB-IV configuration supports in the suspension of solid particles.

Further, CFD - PBE simulations are performed to predict crystal growth and nucleation in the unbaffled and baffled stirred vessel. It is found that the baffled vessel has a uniform local supersaturation and a lower nucleation rate. The effect of seed mass, size and temperature on the CSD was analyzed, and it found that narrow CSD for seed mass of 750g, size of 500 μm and temperature of 308K.

It is found that nucleation, crystal growth and crystal size distribution (KDP) is strongly dependent on local supersaturation, type of stirred vessel, seed amount and temperature distribution in a stirred vessel system. Thus, the hydrodynamics, fluid mixing strongly influence crystal growth (KDP) in stirred vessel system. Besides hydrodynamics and mixing, the quality of the CSD can be improved by using the configuration of the baffled stirred vessel system. Thus, the combined (CFD-PBM) approach helps to understand the crystallization process in a batch stirred vessel system. The predicted results from this study could be important to assure efficient industrial operations of the batch crystallizer.

FUTURE SCOPE

The crystallization phenomena were investigated considering simultaneous growth and nucleation in batch stirred vessel. The following are the future scope

- The phenomena of agglomeration and breakup rate can be included in order to improve the accuracy of the numerical simulations.
- The flow field can be validated experimentally using PIV (Particle Image velocimetry) technique.
- Simulating a reactive crystallization reaction is a challenge in a stirred vessel system due to uncontrolled nucleation and nuclear breeding. This problem can be overcome by understanding micro mixing and controlling the formation of the crystallized product.
- The present simulation methodology can be used to continuous crystallizers to improve the productivity of crystals and uniformity of the CSD.

REFERENCES

- Al-Qaessi, F., and Abu-Farah, L. (2009). "Prediction of mixing time for miscible liquids by CFD simulation in semi-batch and batch reactors." *Engineering Applications of Computational Fluid Mechanics*, 3(1), 135–146.
- Ashraf Ali, B., Börner, M., Peglow, M., Janiga, G., Seidel-Morgenstern, A., and Thévenin, D. (2015). "Coupled computational fluid dynamics-discrete element method simulations of a pilot-scale batch crystallizer." *Crystal Growth and Design*, 15(1), 145–155.
- Ashraf Ali, B., Janiga, G., Temmel, E., Seidel-Morgenstern, A., and Thévenin, D. (2013). "Numerical analysis of hydrodynamics and crystal motion in a batch crystallizer." *Journal of Crystal Growth*, 372, 219–229.
- Ashraf Ali, B., and Pushpavanam, S. (2011). "Analysis of unsteady gas-liquid flows in a rectangular tank: Comparison of Euler-Eulerian and Euler-Lagrangian simulations." *International Journal of Multiphase Flow*, 37(3), 268–277.
- Aubin, J., Mavros, P., Fletcher, D. F., Bertrand, J., and Xuereb, C. (2001). "Effect of Axial Agitator Configuration (Up-Pumping, Down-Pumping, Reverse Rotation) on Flow Patterns Generated in Stirred Vessels." *Chemical Engineering Research and Design*, 79(8), 845–856.
- Aydin, Ö., and Yapici, S. (2018). "A novel method for the measurement of mixing time: A new application of electrochemical limiting diffusion current technique." *Experimental Thermal and Fluid Science*, 99, 242–250.
- Bakker, A., and Fasano, J. (1998). "Time Dependent Turbulent Mixing and Chemical Reactions in Stirred Tanks."
- Baldyga, J., and Bourne, J. R. (1984a). "A fluid mechanical approach to turbulent mixing and chemical reaction part I inadequacies of available methods." *Chemical Engineering Communications*, 28(4–6), 231–241.
- Baldyga, J., and Bourne, J. R. (1984b). "A fluid mechanical approach to turbulent mixing and chemical reaction Part II Micromixing in the light of turbulence theory." *Chemical Engineering Communications*.

Bittorf, K. J., and Kresta, S. M. (2003). "Prediction of cloud height for solid suspensions in stirred tanks." *Chemical Engineering Research and Design*.

Chudacek, M. W. (1985). "Solids suspension behaviour in profiled bottom and flat bottom mixing tanks." *Chemical Engineering Science*, 40(3), 385–392.

Coroneo, M., Montante, G., Paglianti, A., and Magelli, F. (2011). "CFD prediction of fluid flow and mixing in stirred tanks: Numerical issues about the RANS simulations." *Computers & Chemical Engineering*, 35(10), 1959–1968.

Derksen, J. J. (2003). "Numerical Simulation of Solids Suspension in a Stirred Tank." *AIChE Journal*.

Ding, J., and Gidaspow, D. (1990). "A bubbling fluidization model using kinetic theory of granular flow." *AIChE Journal*, 36(4), 523–538.

Doki, N., Kubota, N., Sato, A., and Yokota, M. (2001). "Effect of cooling mode on product crystal size in seeded batch crystallization of potassium alum." *Chemical Engineering Journal*, 81(1–3), 313–316.

Doki, N., Kubota, N., Sato, A., Yokota, M., Hamada, O., and Masumi, F. (1999). "Scaleup experiments on seeded batch cooling crystallization of potassium alum." *AIChE Journal*, 45(12), 2527–2533.

Dong, J., Hu, B., Pacek, A. W., Yang, X., and Miles, N. J. (2016). *The effect of bottom shape and baffle length on the flow field in stirred tanks in turbulent and transitional flow. Int J of Mechanical, Aerospace, Industrial, Mechatronics and Manufacturing Engineering*, Zenodo, 1577–1586.

Fluent Theory Guide. (2013). *Ansys Fluent Theory Guide*. ANSYS Inc., USA.

Fox, R. W., Pritchard, P. J., and McDonald, A. T. (2009). *Introduction To Fluid Mechanics, 7Th Ed*. Wiley India Pvt. Limited.

Galletti, C., Paglianti, A., Lee, K. C., and Yianneskis, M. (2004). "Reynolds number and impeller diameter effects on instabilities in stirred vessels." *AIChE Journal*.

Gao, Z., Rohani, S., Gong, J., and Wang, J. (2017). "Recent Developments in the Crystallization Process: Toward the Pharmaceutical Industry." *Engineering*, 3(3), 343–353.

Gidaspow, D., Bezburuah, R., and Ding, J. (1992). “Hydrodynamics of Circulating Fluidized Beds.” *Fluidization VII, Proceedings of the 7th Engineering Foundation Conference on Fluidization*.

Gidaspow, D., Shih, Y. -T, Bouillard, J., and Wasan, D. (1989). “Hydrodynamics of a lamella electrosettler.” *AIChE Journal*, 35(5), 714–724.

Green, D. (2002). “Crystallizer mixing.” *Handbook of Industrial Crystallization*, 181–199.

Hemalatha, K., and Rani, K. Y. (2017). “Multiobjective Optimization of Unseeded and Seeded Batch Cooling Crystallization Processes.” *Industrial and Engineering Chemistry Research*.

Hicks, M. T., Myers, K. J., and Bakker, A. (1997). “Cloud height in solids suspension agitation.” *Chemical Engineering Communications*.

Houcine, I., Plasari, E., and David, R. (2000). “Effects of the Stirred Tank’s Design on Power Consumption and Mixing Time in Liquid Phase.” *Chemical Engineering & Technology*, 23(7), 605–613.

John, V., Angelov, I., Öncül, A. A., and Thévenin, D. (2007). “Techniques for the reconstruction of a distribution from a finite number of its moments.” *Chemical Engineering Science*.

Joshi, J. B., Nere, N. K., Rane, C. V., Murthy, B. N., Mathpati, C. S., Patwardhan, A. W., and Ranade, V. V. (2011). “CFD simulation of stirred tanks: Comparison of turbulence models. Part I: Radial flow impellers.” *The Canadian Journal of Chemical Engineering*, 89(1), 23–82.

Kasat, G. R., Khopkar, A. R., Ranade, V. V., and Pandit, A. B. (2008). “CFD simulation of liquid-phase mixing in solid–liquid stirred reactor.” *Chemical Engineering Science*, 63(15), 3877–3885.

Kougoulos, E., Jones, A. G., and Wood-Kaczmar, M. (2005). “CFD modelling of mixing and heat transfer in batch cooling crystallizers aiding the development of a hybrid predictive compartmental model.” *Chemical Engineering Research and Design*, 83(1 A), 30–39.

- Kramer, H. J. ., Bermingham, S. K., and Rosmalen, G. M. van. (1999). “Design of industrial crystallisers for a given product quality.” *Journal of Crystal Growth*, 198–199, 729–737.
- Krishnaveni, T., Renganathan, T., Picardo, J. R., and Pushpavanam, S. (2017). “Numerical study of enhanced mixing in pressure-driven flows in microchannels using a spatially periodic electric field.” *Physical Review E*, 96(3), 33117.
- Kubota, N., and Onosawa, M. (2009). “Seeded batch crystallization of ammonium aluminum sulfate from aqueous solution.” *Journal of Crystal Growth*, 311(20), 4525–4529.
- Kumaresan, T., and Joshi, J. B. (2006). “Effect of impeller design on the flow pattern and mixing in stirred tanks.” *Chemical Engineering Journal*, 115(3), 173–193.
- Launder, B. E., and Spalding, D. B. (1972). *Lectures in Mathematical Models of Turbulence*. Academic Press.
- Lewis, A., Seckler, M., Kramer, H., and Rosmalen, G. Van. (2015). *Industrial crystallization: fundamentals and applications*. Cambridge University Press.
- Liiri, M., Hatakka, H., Kallas, J., Aittamaa, J., and Alopaeus, V. (2010). “Modelling of crystal growth of KDP in a 100dm³ suspension crystallizer using combination of CFD and multiblock model.” *Chemical Engineering Research and Design*, 88(9), 1297–1303.
- Lun, C. K. K., Savage, S. B., Jeffrey, D. J., and Chepurniy, N. (1984). “Kinetic theories for granular flow: Inelastic particles in Couette flow and slightly inelastic particles in a general flowfield.” *Journal of Fluid Mechanics*.
- Ma, D., and Ahmadi, G. (1990). “A thermodynamical formulation for dispersed multiphase turbulent flows-II. Simple shear flows for dense mixtures.” *International Journal of Multiphase Flow*.
- Madana, V. S. T., and Ashraf Ali, B. (2020). “Numerical investigation of engulfment flow at low Reynolds numbers in a T-shaped microchannel.” *Physics of Fluids*, 32(7), 072005.
- Marchisio, D. L., Vigil, R. D., and Fox, R. O. (2003). “Implementation of the quadrature

- method of moments in CFD codes for aggregation–breakage problems.” *Chemical Engineering Science*, 58(15), 3337–3351.
- Marshall, E. M., and Bakker, A. (2003). “Computational Fluid Mixing.” *Handbook of Industrial Mixing*, Wiley Online Books.
- McGraw, R. (1997). “Description of aerosol dynamics by the quadrature method of moments.” *Aerosol Science and Technology*.
- Mendoza-Escamilla, V. X., Alonzo-García, A., Mollinedo, H. R., González-Neria, I., Antonio Yáñez-Varela, J., and Martínez-Delgadillo, S. A. (2018). “Assessment of $k-\epsilon$ models using tetrahedral grids to describe the turbulent flow field of a PBT impeller and validation through the PIV technique.” *Chinese Journal of Chemical Engineering*, 26(5), 942–956.
- Meroney, R. N., and Colorado, P. E. (2009). “CFD simulation of mechanical draft tube mixing in anaerobic digester tanks.” *Water Research*.
- Mersmann, A. (2001). *Crystallization Technology Handbook - Second Edition Revised and Expanded*. Marcel Dekker Inc.
- Mishra, P., and Ein-Mozaffari, F. (2020). “Critical review of different aspects of liquid-solid mixing operations.” *Reviews in Chemical Engineering*, 36(5), 555–592.
- Moliner, C., Marchelli, F., Spanachi, N., Martínez-Felipe, A., Bosio, B., and Arato, E. (2019). “CFD simulation of a spouted bed: Comparison between the Discrete Element Method (DEM) and the Two Fluid Model (TFM).” *Chemical Engineering Journal*, 377, 120466.
- Mullin, J. W. (2001). *Crystallization*. Elsevier.
- Myerson, A. S., Erdemir, D., and Lee, A. Y. (2019). *Handbook of industrial crystallization. Handbook of Industrial Crystallization*, Butterworth-Heinemann.
- Ochieng, A., and Lewis, A. E. (2006). “CFD simulation of solids off-bottom suspension and cloud height.” *Hydrometallurgy*.
- Ochieng, A., and Onyango, M. S. (2008). “Homogenization energy in a stirred tank.” *Chemical Engineering and Processing: Process Intensification*, 47(9–10), 1853–1860.
- Ochieng, A., and Onyango, M. S. (2010). “CFD simulation of solids suspension in

stirred tanks: Review.” *Hemijaska Industrija*.

Ochieng, A., Onyango, M. S., Kumar, A., Kiriamiti, K., and Musonge, P. (2008). “Mixing in a tank stirred by a Rushton turbine at a low clearance.” *Chemical Engineering and Processing: Process Intensification*, 47(5), 842–851.

Öncül, A. A., Niemann, B., Sundmacher, K., and Thévenin, D. (2006). “CFD model of a semi-batch reactor for the precipitation of nanoparticles in the droplets of a microemulsion.” *Computer Aided Chemical Engineering*, 21(C), 203–208.

Oshinowo, L., Bakker, A., and Marshall, E. (2002). “Computational fluid dynamics: Simulating mixing time.” *Chemical Engineering World*, 37(7), 75–77.

Oshinowo, L. M., and Bakker, A. (2001). “CFD modeling of solids suspensions in stirred tanks.” *Computational Modeling of Materials, Minerals and Metals Processing*.

Patwardhan, A. W., and Joshi, J. B. (1999). “Relation between Flow Pattern and Blending in Stirred Tanks.” *Industrial & Engineering Chemistry Research*, 38(8), 3131–3143.

Paul, E. L., Midler, M., and Sun, Y. (2004). *Mixing in the Fine Chemicals and Pharmaceutical Industries. Handbook of Industrial Mixing*.

Ranade, V. V., Mishra, V. P., Saraph, V. S., Deshpande, G. B., and Joshi, J. B. (1992). “Comparison of Axial Flow Impellers Using a Laser Doppler Anemometer.” *Industrial and Engineering Chemistry Research*, 31(10), 2370–2379.

Rane, C. V., Ganguli, A. A., Kalekudithi, E., Patil, R. N., Joshi, J. B., and Ramkrishna, D. (2014). “CFD simulation and comparison of industrial crystallizers.” *Canadian Journal of Chemical Engineering*, 92(12), 2138–2156.

Richards, A. (2012). “Introduction to the Special Issue on the Head and Neck.” *Clinical Anatomy*, 25(1), 1–1.

Rohani, S., Horne, S., and Murthy, K. (2005a). “Control of product quality in batch crystallization of pharmaceuticals and fine chemicals. Part 1: Design of the crystallization process and the effect of solvent.” *Organic Process Research and Development*, 9(6), 858–872.

Rohani, S., Horne, S., and Murthy, K. (2005b). “Control of Product Quality in Batch

Crystallization of Pharmaceuticals and Fine Chemicals. Part 2: External Control.” *Organic Process Research & Development*, 9(6), 873–883.

Sahu, A. K., Kumar, P., Patwardhan, A. W., and Joshi, J. B. (1999). “CFD modelling and mixing in stirred tanks.” *Chemical Engineering Science*, 54(13–14), 2285–2293.

Sommerfeld, M., and Decker, S. (2004). “State of the art and future trends in CFD simulation of stirred vessel hydrodynamics.” *Chemical Engineering and Technology*, 27(3), 215–224.

Souza, L. M. de, Temmel, E., Janiga, G., Seidel-Morgenstern, A., and Thévenin, D. (2021). “Simulation of a batch crystallizer using a multi-scale approach in time and space.” *Chemical Engineering Science*, 232, 116344.

Srinivasa, T., and Jayanti, S. (2007). “An eulerian/lagrangian study of solid suspension in stirred tanks.” *AIChE Journal*, 53(9), 2461–2469.

Sulttan, S., and Rohani, S. (2019). “Coupling of CFD and population balance modelling for a continuously seeded helical tubular crystallizer.” *Journal of Crystal Growth*, 505, 19–25.

Szilágyi, B., and Nagy, Z. K. (2018). “Population Balance Modeling and Optimization of an Integrated Batch Crystallizer-Wet Mill System for Crystal Size Distribution Control.” *Crystal Growth and Design*, 18(3), 1415–1424.

Tamburini, A., Cipollina, A., Micale, G., Brucato, A., and Ciofalo, M. (2014). “Influence of drag and turbulence modelling on CFD predictions of solid liquid suspensions in stirred vessels.” *Chemical Engineering Research and Design*, 92(6), 1045–1063.

Tamburini, A., Cipollina, A., Micale, G., Ciofalo, M., and Brucato, A. (2009). “Dense solid-liquid off-bottom suspension dynamics: Simulation and experiment.” *Chemical Engineering Research and Design*, 87(4), 587–597.

Tatterson, G. B. (1982). “The effect of draft tubes on circulation and mixing times.” *Chemical Engineering Communications*, 19(1–3), 141–147.

Temmel, E., Eicke, M., Lorenz, H., and Seidel-Morgenstern, A. (2016a). “A Short-Cut Method for the Quantification of Crystallization Kinetics. 2. Experimental

Application.” *Crystal Growth & Design*, 16(12), 6756–6768.

Temmel, E., Eisenschmidt, H., Lorenz, H., Sundmacher, K., and Seidel-Morgenstern, A. (2016b). “A Short-Cut Method for the Quantification of Crystallization Kinetics. 1. Method Development.” *Crystal Growth and Design*, 16(12), 6743–6755.

Torotwa, I., and Ji, C. (2018). “A study of the mixing performance of different impeller designs in stirred vessels using computational fluid dynamics.” *Designs*, 2(1), 10.

Vedantam, S., and Ranade, V. V. (2013). “Crystallization: Key thermodynamic, kinetic and hydrodynamic aspects.” *Sadhana - Academy Proceedings in Engineering Sciences*, 38(6), 1287–1337.

Visuri, O., Liiri, M., and Alopaeus, V. (2011). “Comparison and validation of CFD models in liquid-solid suspensions.” *Canadian Journal of Chemical Engineering*, 89(4), 696–706.

Wan, B., and Ring, T. A. (2006). “Verification of SMOM and QMOM population balance modeling in CFD code using analytical solutions for batch particulate processes.” *China Particuology*, 4(5), 243–249.

Wan, B., Ring, T. A., Dhanasekharan, K. M., and Sanyal, J. (2005). “Comparison of analytical solutions for cmsmpr crystallizer with QMOM population balance modeling in fluent.” *China Particuology*, 3(4), 213–218.

Wei, H., Zhou, W., and Garside, J. (2001). “Computational fluid dynamics modeling of the precipitation process in a semibatch crystallizer.” *Industrial and Engineering Chemistry Research*, 40(23), 5255–5261.

Weinekötter, R., and Gericke, H. (2013). *Mixing of solids*. Springer Science & Business Media.

Wendt, J. F., Anderson, J. D., Degroote, J., Degrez, G., Dick, E., Grundmann, R., and Vierendeels, J. (2009). *Computational fluid dynamics: An introduction. Computational Fluid Dynamics*.

Wu, B. (2014). “CFD simulation of gas mixing in anaerobic digesters.” *Computers and Electronics in Agriculture*.

Yoshida, M., Ebina, H., Shirosaki, H., Ishioka, K., and Oiso, K. (2015). “Liquid flow

in impeller swept regions of baffled and unbaffled vessels with a turbine-type agitator.”
Brazilian Journal of Chemical Engineering, 32(4), 865–873.

Zhou, G., and Kresta, S. M. (1996). *Distribution of energy between convective and turbulent flow for three frequently used impellers*. *Chemical Engineering Research and Design*.

APPENDIX – I

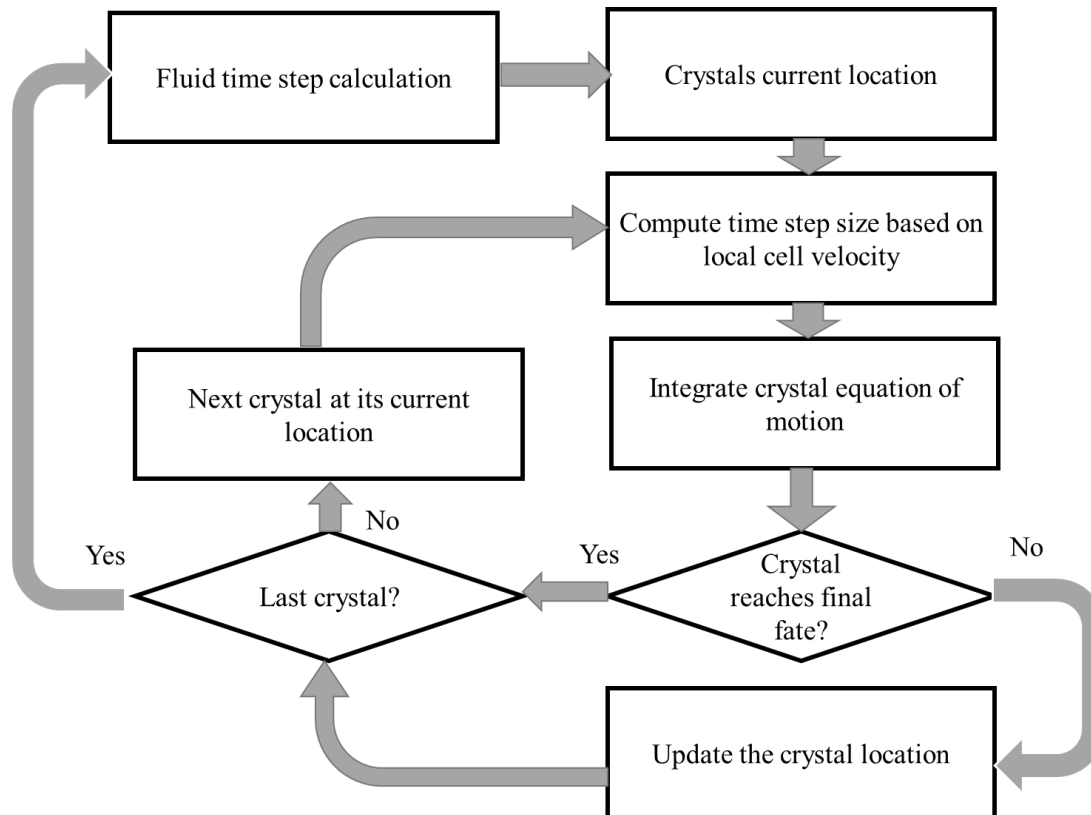
Numerical procedure to calculate hydrodynamics and crystal growth calculation
The commercial software (ANSYS Fluent 2020R1) is used in this research work through the inbuilt implementation of QMOM. The algorithm for the PBE-Euler-Granular model is explained sequentially

1. Intialise the solution with the values of six moments, particulate volume fraction, solution temperature, concentration of the solute and mass of the seeds
2. Solve the Euler -granular (multifluid) equations, using the Sauter mean diameter ($d_{32} = \mu_3/\mu_2$) obtained from the moments
3. Solve the PBE using the moment-inversion algorithm PDA to generate QMOM values: i.e. the weights and abscissas of the CSD
4. Calculate the source terms i.e., nucleation rate and growth rate due to mass transfer.
5. Solve the moment transport equations, using velocity field obtained from the Euler granular model.
6. Repeat the steps 2 to 5 for each time step,

APPENDIX – II

Numerical procedure to calculate Shannon entropy through DPM simulations

DPM Calculations for unsteady flow



The liquid (continuous) and crystal (discrete) phase is two way coupled. The flow field is solved first for the continuous phase. Then particles are injected at the top of the vessel and the trajectories are calculated based on the predicted continuous flow field. Further the flow field of the continuous phase is updated based on the exchange of momentum between the two phases. Finally, the discrete phase trajectories are predicted based on this modified flow field.

The distribution and mixing of the particles in the vessel are quantified using Shannon entropy. The volume of interest is divided into many equally sized volumes called bins. The probability (p_k) of the number of particles in each bin is calculated. The information of the location of the particles is obtained from the particle data at the end of the DPM simulations. Finally, the Shannon's entropy (S) is obtained by calculating the probability distribution of particles in each bin. The magnitude of the Shannon's entropy indicates the distribution of the particles in the vessel.

APPENDIX - III

A. User-defined function for nucleation rate of KDP

```
/* Negated forms that are more commonly used */
/*****/

#if !RP_HOST
/* either serial or compute node process is involved */
#endif
/*****/

UDF that computes the particle nucleation rate
*****/

#include "udf.h"
#include "sg_pb.h"
#include "sg_mphase.h"

DEFINE_PB_NUCLEATION_RATE(nuc_rate, cell, thread)
{
    real SS;
    real J;
    real p1 = 0.052; /* nuc constant */
    real p2 = 1000.; /*nuc const activation energy constant J/mol */
    real p3 = 5.8; /* nucleation law power index */
    real R = 8.314; /*gas constant j/mol.k*/
    real T, T1, solute_mass_frac, solubility, solubility_mass;
    real solute_mol_wt, solvent_mol_wt;
    Thread *tc = THREAD_SUPER_THREAD(thread); /*obtain mixture thread */
    Thread **pt = THREAD_SUB_THREADS(tc); /* pointer to sub_threads */
    Thread *tp = pt[P_PHASE]; /* primary phase thread */
    solute_mol_wt = 136.0; /* molecular weight of kdp */
    solvent_mol_wt = 18.; /* molecular weight of water */
    solute_mass_frac = C_YI(cell,tp,0); /* mass fraction of solute in primary phase
(solvent) */
    T1 = C_T(cell,tp); /* Temperature of primary phase in Kelvin */
}
```

```

T = (T1-273.15); /* Temperature of primary phase in degree Celcius */
solubility_mass = 15.24+(2.06*0.1*T)+(1.01*0.01*pow(T,2))-
(1.45*0.0001*pow(T,3))+1.23*0.000001*pow(T,4); /* mass solubility in
percentage*/
solubility = (solubility_mass/100.0); /* Solubility Law relating equilibrium solute
mole fraction to Temperature*/
SS = solute_mass_frac/solubility; /* Definition of Supersaturation */
if (SS <= 1.)
{
J = 0.;
}
else
{
J = p1*exp(-p2/(R*T1))*pow((SS-1),p3);
C_UDMI(cell,tc,2) = J;
/* saving local nucleation rate to memory */
C_UDMI(cell,tc,0) = SS;
/* saving local supersaturation to memory */

}
return J;
}
/*****/

```

B. User-defined function for the growth rate of KDP

```

/*****/
/* Negated forms that are more commonly used */
/*****/
#if !RP_HOST
/* either serial or compute node process is involved */
#endif
/*****/
UDF that computes the particle growth rate

```

```

/*****/
#include "udf.h"
#include "sg_pb.h"
#include "sg_mphase.h"
DEFINE_PB_GROWTH_RATE(growth_rate, cell, thread, d_1)
{
/* d_1 can be used if size-dependent growth is needed */
/* When using SMM, only size-independent or linear growth is allowed */
real SS;
real G;
real p1 = 5100000; /* growth constant */
real p2 = 70000.0; /*activation energy J/mol */
real p3 = 1.26; /* growth law power index */
real R = 8.314; /*gas constant J/mol.k*/
real kv =0.75; /* shape factor*/
real T, T1, solute_mass_frac, solubility;
real solute_mol_wt, solvent_mol_wt, solubility_mass;
Thread *tc = THREAD_SUPER_THREAD(thread); /*obtain mixture thread */
Thread **pt = THREAD_SUB_THREADS(tc); /* pointer to sub_threads */
Thread *tp = pt[P_PHASE]; /* primary phase thread */
solute_mol_wt = 136.0; /* molecular weight of potassium dihydrogen phosphate
*/
solvent_mol_wt = 18.0; /* molecular weight of water */
solute_mass_frac = C_YI(cell, tp, 0); /* mass fraction of solute in primary phase
(solvent) */
T1 = C_T(cell,tp); /* Temperature of primary phase in Kelvin */
T = (T1-273.15); /* Temperature of primary phase in degree Celcius */
solubility_mass = 15.24+(2.06*0.1*T)+(1.01*0.01*pow(T,2))-
(1.45*0.0001*pow(T,3))+1.23*0.000001*pow(T,4); /* mass solubility in
percentage*/
solubility = (solubility_mass/100.0); /* Solubility Law relating equilibrium solute
mole fraction to Temperature*/

```

```

SS = solute_mass_frac/solubility; /* Definition of Supersaturation */
if (SS <= 1.)
{
G = 0.;
}
else
{
G = kv*p1*exp(-p2/(R*T1))*pow((SS-1),p3);
C_UDMI(cell,tc,1) = G;
/* saving local growth rate to memory */
}
return G;
}
/*****/

```

RESEARCH PUBLICATIONS

PEER-REVIEWED JOURNAL PUBLICATIONS (SCI)

- Lister H. Falleiro & Basheer Ashraf Ali (2021) Computational modeling of hydrodynamics and mixing in a batch stirred vessel, *Chemical Engineering Communications*, 208:6, 883-892, DOI: 10.1080/00986445.2019.1694919
- Basheer Ashraf Ali & Lister H. Falleiro (2021) “Effect of baffle configuration on performance of batch stirred vessel”, *Korean journal of Chemical Engineering*, - **(Under review)**
- Lister H. Falleiro & Basheer Ashraf Ali (2020) “Numerical investigation of crystal growth in a batch crystallizer using coupled CFD-PBE approach”, Springer Nature, - **(Under review)**

PEER-REVIEWED JOURNAL PUBLICATIONS (non-SCI)

- Thimmaiah, A., Falleiro, L., Naval, A., Ambekar, A., and Ali, B. A. (2016). “Numerical Analysis of Flow Characterization in a Continuous Crystallizer.” *IJCST*, 2(2), 33–43. DOI:10.13140/RG.2.2.24846.77125
- Falleiro L., Ali, B. A (2017) “Numerical investigation of hydrodynamics of batch crystallizer” *International Journal of Chemical Engineering and Processing*, 3(1) 24-35.

CONFERENCE PRESENTATIONS

- Lister H F, B Ashraf Ali (2019). “CFD modelling of hydrodynamics and mixing in a batch stirred vessel” *Proceedings of Recent Advancements in Chemical, Environmental and Energy Engineering (RACEEE 2019)*, during 14-15, Feb 2019 at SSN College of Engineering Chennai
- Lister H F, B Ashraf Ali (2019). “Population balance modelling of a batch crystallizer” *Proceedings of International Symposium on Modelling of Crystal Growth Processes and Devices (MCGPD-2019)*, during 26-28, Feb 2019 at SSN College of Engineering Chennai. **(Awarded as the best paper in the conference)**
- Lister H F, B Ashraf Ali (2019). “PBM coupled CFD simulation of batch crystallizer” *Proceedings of the 46th National Conference on Fluid Mechanics and*

Fluid Power (FMFP), during 9-11, Dec 2019, at PSG College of Technology,
Coimbatore, India.

BIODATA

Lister Herington Falleiro

Belgaum Karnataka India

Mob: +91- 8951047884

E-mail: hfalleiro@gmail.com

EPMC Work Experience

Designation: **Process Engineer** (Process Department)

Experience: **1 year, 8 months (Dec 2013 – July 2015)**

Organization: **Jacobs Engineering India Pvt. Ltd** Mumbai

EPMC Work Experience

Designation: **Assistant Manager** (Process Department)

Experience: **5 years, 4 months (Aug 2008 – Dec 2013)**

Organization: **Tata Consulting Engineers Ltd (TCE)** Mumbai.

Job Responsibilities

Involved in following Process Engineering activities:

1. Preparation of Conceptualization / **Basic Study**
2. Preparation of **Process Flow diagram (PFD)**
3. **Line sizing** and **Hydraulic** calculations
4. Preparation of **Piping & Instrumentation Diagram (P&ID)**
5. **Pump hydraulic** calculations and Pump sizing
6. Preparation of **Electrical Load list**. (EDL)
7. Preparation of **Pump Datasheets, Tank Datasheets, Heat Exchanger Datasheets**
8. Preparation of Process **Instrument Datasheets**, Control Valve datasheets
9. Preparation of **Line Designation Schedule (LDS)**
10. Participation in **HAZOP** Studies
11. Well conversant of **API and OISD** Standards
12. Preparation of **Equipment layout** drawing
13. **Co-ordinating** with inter-disciplinary departments.
14. Preparation of **Enquiry / Tender Specification** for the packages
15. **Interacting and Corresponding** with Client and Vendors.

16. **Technical Bid analysis (TBA)** after receipt of the BIDs from Bidder's.
17. **Reviewing / Commenting** on Vendor drawings and documents received.
18. **Internal Auditor** for Quality Management System (QMS) in the company – Certified ISO 9001: 2008 Internal Auditor.

Production Work Experience

Designation: Management Trainee (**Chemical**)

Experience: **8 months (Oct 2005 – Jul 2006)**

Organization: **Riddhi Siddhi Gluco Biols Limited.**

Job Responsibilities

1. Responsible for supervising the plant and process at optimal conditions to meet the planned target.
2. Corrective and preventive actions for abnormal situations.
3. Co-coordinating maintenance activities with respective functions and provide process support.
4. Reporting production, attending to the maintenance problems during the shift.
5. Good exposure to unit process & unit operations like Continuous plug flow reactors, batch reactors, stirred vessels, scrapper crystallizer, ion exchange column, conveying systems, spray dryer, rotary vacuum filters, filter press, multistage evaporation, water treatment plant and effluent treatment plant.

ACADEMIC RECORD:

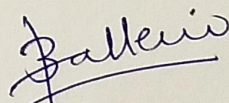
Degree	Specialization	% Marks / CGPA	Year	School / College
Ph. D	Chemical Engineering	7.3	2021	N.I.T Karnataka
M. Tech	Industrial Pollution Control	7.78	2008	N.I.T Karnataka
B. E	Chemical Engineering	79.2%	2005	KLECET Belgaum
PUC II	Science	72.0%	2001	St. Xavier's PUC
S.S.L.C	English	68%	1999	St. Paul's High School

Achievements

1. Simulated process problems using simulation **software** like **ANSYS Fluent 2021R1, MATLAB, CHEMCAD v5.5, HTRI v7.0** and **HYSYS v3.5**.
2. I have excelled in the Software skills of **MS office 2019** and **AutoCAD 2012**.
3. Prepared a comprehensive report on “**Hazardous Waste Management in Karnataka**“, at **Karnataka State Pollution Control Board, Bangalore**, during the year 2007
4. Presented State level paper presentation on “**HAZOP studies on Sulphuric acid Industry**” at BIET Davangere in 2004.
5. Presented and won the **second prize, National level** paper presentation on “**An Electrochemical Approach to the Studies of Bio-based Redox Reactions**” at BIET Davangere Karnataka in 2007
6. Completed **ISO 9001: 2008** course and conducted **7** internal Audits
7. Completed **Basic Fire Fighting** course.
8. I was the **Safety Coordinator** for the process department, and floor Leader in case of fire emergency and evacuation

Declaration

I hereby declare that all information given above is true, correct and complete according to the best of my knowledge and belief.



Lister Herington Falleiro